

Determination of the beam asymmetry Σ in η - and η' -photoproduction using Bayesian statistics

JAKOB MICHAEL KRAUSE

Masterarbeit in Physik

angefertigt im Helmholtz-Institut für Strahlen- und
Kernphysik

vorgelegt der

Mathematisch-Naturwissenschaftlichen Fakultät
der
Rheinischen Friedrich-Wilhelms-Universität
Bonn

Sep 2022

DRAFT

I hereby declare that this thesis was formulated by myself and that no sources or tools other than those cited were used.

Bonn,
Date
Signature

1. Gutachterin: JUN. PROF. DR. ANNIKA THIEL
2. Gutachter: PROF. DR. JOCHEN DINGFELDER

DRAFT

Contents

1	Introduction	1
1.1	Photoproduction of Pseudoscalar Mesons	4
1.2	Measurement of Polarization Observables	5
1.3	Introduction to BAYESIAN statistics	5
1.3.1	Frequentist Approach	5
1.3.2	Bayesian approach	5
1.3.3	Combining inferences	5
1.4	Motivation and Structure of this Thesis	5
2	Experimental Setup	7
2.1	Production of polarized high energy photon beam	8
2.1.1	Goniometer	9
2.1.2	Tagging system	9
2.2	Liquid hydrogen target	10
2.3	Detector system	11
2.3.1	Inner detector	11
2.3.2	Crystal Barrel and forward detector	12
2.3.3	MiniTAPS	13
2.3.4	ČERENKOV detector	14
2.3.5	Flux monitoring	14
2.4	Trigger	15
2.5	Software and Monte Carlo	15
2.5.1	ExPLORA	16
2.5.2	Monte Carlo	16
2.5.3	Stan	17
2.6	Datasets	17
3	Event selection	19
3.1	Reconstruction of events	20
3.2	Preselection and charge cut	20
3.3	Time of particles	21
3.4	Kinematic constraints	23
3.4.1	Derivation of cut conditions	23
3.4.2	Determination of cut ranges	24
3.4.3	Quality of event selection	29

3.5	Investigation of background and additional cuts	31
3.5.1	Inspecting plausibility of background reactions	31
3.5.2	Misidentification of background reactions	34
3.5.3	Examination of additional cuts	39
3.6	Summary of event selection	42
3.6.1	Reaction $\gamma p \rightarrow p\eta' \rightarrow p\gamma\gamma$	42
3.6.2	Reaction $\gamma p \rightarrow p\eta \rightarrow p\gamma\gamma$	43
4	Extraction of the beam asymmetries Σ_η and $\Sigma_{\eta'}$	37
4.1	Methods	38
4.1.1	Event yield asymmetries	38
4.1.2	Event based fit	41
4.2	Determination of Σ_η using Bayesian statistics	44
4.2.1	Application of methods to toy Monte Carlo data	44
4.2.2	Application of methods to data	53
4.2.3	Discussion	56
4.3	Determination of $\Sigma_{\eta'}$	58
4.3.1	Application of event based fit to toy Monte Carlo data	58
4.3.2	Application of event based fit to data	64
4.3.3	Systematic error	68
5	Discussion of results	73
5.1	Comparison of results to existing data	73
5.2	Comparison of results to PWA calculations	75
5.3	Final discussion of methods	77
5	Summary and outlook	73
A	Illustration of used software tools	75
A.1	ExPLORA	75
A.2	Stan	76
B	Additional plots and calculations	77
B.1	Statistical error for the asymmetry $A(\phi)$	77
B.2	Kinematic variables for each bin	79
B.2.1	Coplanarity	79
B.2.2	Polar angle difference	81
B.2.3	Missing mass	83
B.2.4	Invariant mass	85
C	Discussion of binned fits	87
D	Investigation of posteriors without truncation	89
	Bibliography	93

List of Figures	97
List of Tables	103

DRAFT

DRAFT

CHAPTER 2

Experimental Setup

In this work the beam asymmetry Σ is determined in the reactions $\gamma p \rightarrow p\eta$ and $\gamma p \rightarrow p\eta'$, requiring a polarized photon beam and an unpolarized proton target. It is convenient to study photoproduction off a fixed target and investigate the resonances that occur in the process. The analyzed data was taken at the CBELSA/TAPS experiment located in Bonn at the EElectron Stretcher Accelerator (ELSA). In this chapter the different parts of the CBELSA/TAPS experiment that are used for the measurement of the beam asymmetry Σ will be presented. Figure 2.1 shows an overview of the experimental hall. All mentioned parts are discussed in detail in the following High energy electrons extracted from ELSA

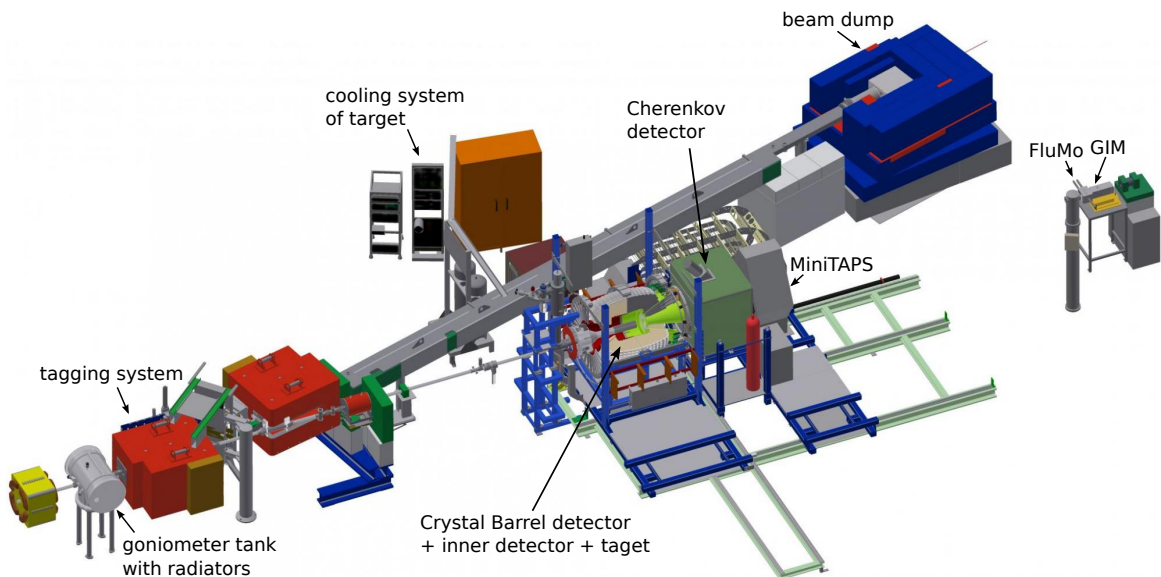


Figure 2.1: Overview of the experimental hall of the CBELSA/TAPS experiment. The electron beam from ELSA enters at the top right. M. GRÜNER in [Afz19]

are used to produce a polarized photon beam using the *bremssstrahlung* process (see 2.1.1). After they have been energy tagged (see 2.1.2) these photons then interact with the fixed target material (see Section 2.2) so that hadronic resonances may be excited that will decay via the strong interaction

under the emission of mesons. The resulting decay products can then be measured with a system of electromagnetic calorimeters and scintillators that is especially suited for the detection of photons (see Section 2.3). The analogue measurements are only saved for offline analysis if detector signals meet certain trigger conditions which is only the case for reactions that are of interest (see Section 2.4). This way the amount of unwanted background is minimized already during the process of data taking. Once data acquisition is finished the data may be investigated with the help of analysis software and Monte Carlo simulations tailored to the needs of the CBELSA/TAPS experiment (see Section 2.5).

2.1 Production of polarized high energy photon beam

To measure polarization observables in photoproduction reactions a polarized photon beam is needed which can be created using *coherent bremsstrahlung*. Bremsstrahlung is the dominating interaction of high energy ($\mathcal{O}(1 \text{ GeV})$) electrons with matter [Leo94]. Electrons are decelerated in the COLOUMB field of heavy nuclei and radiate real photons, see Figure 2.2.

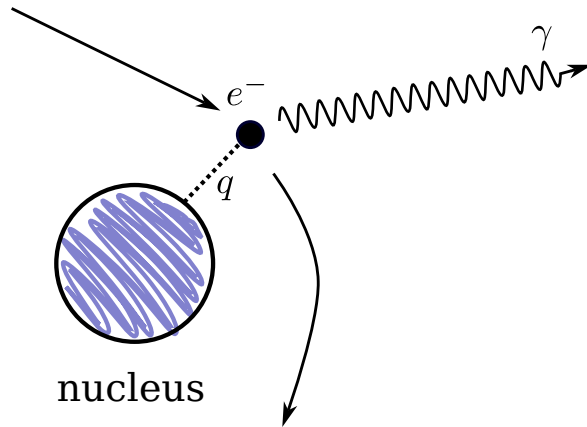


Figure 2.2: Illustration of the bremsstrahlung process: An electron e^- is deflected in the COLOUMB field of a nucleus in the radiator material. A photon γ is emitted and so the momentum q is transferred.

To conserve momentum there has to be a momentum transfer q which is negligibly small compared to the nucleon mass. If an amorphous radiator is used incoherent bremsstrahlung is produced with a continuous spectral distribution proportional to $1/E_\gamma$, according to the BETHE-HEITHLER cross section [Hei54]. Since the structure of nuclei in the amorphous radiator does not exhibit any periodicity, the electric field vector will not prefer any particular direction, resulting in a net polarization degree of zero for the photon beam. To achieve non-vanishing polarization degrees a crystal with periodic placement of nuclei may be used as radiator. Then, coherent bremsstrahlung is produced; the crystal can absorb the recoil only for discrete momenta q_n meeting the LAUE condition [Dem10] of the crystal lattice. This enables constructive interference between different bremsstrahl photons and at the same time fixes the deflection plane of incoming electrons, resulting in a coherent polarized photon beam. Incoherent bremsstrahlung may still occur due to impurities in the crystal structure, so that the total bremsstrahlung cross section off a crystal radiator σ_{crystal} is the sum of a coherent (σ_{coherent}) and an incoherent ($\sigma_{\text{incoherent}}$) part

$$\sigma_{\text{crystal}} = \sigma_{\text{coherent}} + \sigma_{\text{incoherent}}. \quad (2.1)$$

The process of bremsstrahlung can be modeled using ANalytical Bremsstrahlung (ANB) calculations [Nat+03]. ANB intensity spectra for a crystal and amorphous radiator are shown in Figure 2.3 on the left hand side. The right hand side shows the enhancement spectrum, which is given by dividing the two spectra. One observes that the bremsstrahlung intensity spectrum obtained from a crystal radiator

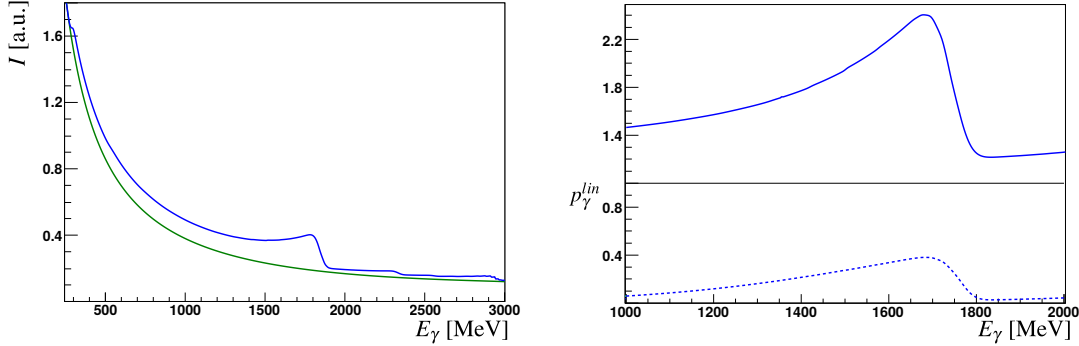


Figure 2.3: Left: Incoherent (green) and crystal (blue) bremsstrahlung intensities as a function of the photon energy. Right: The enhancement spectrum is given as the ratio of crystal to incoherent intensity spectrum. The dashed line at the bottom shows the calculated polarization degree. Both spectra are generated using ANB calculations. Taken from [Afz19].

is in general enhanced relative to the incoherent spectrum obtained from an amorphous radiator. In fact, using ANB calculations, the polarization degree can be determined from the enhancement spectrum. The characteristic drop in intensity in the intensity spectrum obtained from the crystal radiator is referred to as the coherent edge. It occurs because the photon energy in the kinematically allowed region of the recoil momentum that will lead to coherent bremsstrahlung is limited. The relative alignment of the radiation crystal to the electron beam determines the position of the coherent edge.

2.1.1 Goniometer

In order to determine the beam polarization from enhancement spectra, a diamond radiator as well as an amorphous radiator are required. Several radiators as well as beam diagnostics tools mounted inside a rotating aluminum wheel are part of the goniometer [Els+09], resting inside a vacuum tank. Depending on whether linearly polarized or unpolarized photons are needed either copper radiators of different thickness or a diamond radiator, which is located in the center of the wheel, are inserted into the beam axis, see Figure 2.4. In case a circularly polarized photon beam is required, a MØLLER polarimeter [Kam10] is used, which is also shown in Figure 2.4. The goniometer can be rotated in all directions allowing precise alignment with the incoming electron beam from ELSA.

2.1.2 Tagging system

Once the impinging electrons from ELSA have scattered off the radiator their energy is determined in order to measure the energy of the created photons. This is possible because the initial electron energy $E_0 = 3.2 \text{ GeV}$ is known from ELSA. Thus, the photon Energy E_γ is given by subtracting the

energy of the recoil electrons E_e from E_0 ¹

$$E_\gamma = E_0 - E_e. \quad (2.2)$$

The recoiling electrons are deflected towards the tagging system [For10] consisting of 96 overlapping scintillator bars and 480 scintillating fibers using the magnetic field of a dipole magnet with a field strength of 1.5 T. The bending radius of the electrons depends on their momenta is uniquely defined by the tagger hit position. With the position of the deflected electrons and the magnetic field strength, E_e can thus be determined. For an initial energy $E_0 = 3.2$ GeV the scintillator bars cover an energy range of $560\text{ MeV} < E_\gamma < 3100\text{ MeV}$ with an energy resolution of $0.1\%E_\gamma$ - $6\%E_\gamma$. The fibers additionally improve the energy resolution in the energy range $416\text{ MeV} < E_\gamma < 2670\text{ MeV}$ to $0.1\%E_\gamma$ - $0.4\%E_\gamma$. Photomultipliers are used for the readout of the tagger bars and fibers, realizing a time resolution of $^2\text{FWHM}_{\text{bar}} = 635\text{ ps}$ and $\text{FWHM}_{\text{fiber}} = 1.964\text{ ns}$ [Har08]. Any electrons that have not interacted with the radiator material are deflected by another dipole magnet towards the beam dump, see Figure 2.1. Figure 2.5 shows a top-down view of the tagging system.

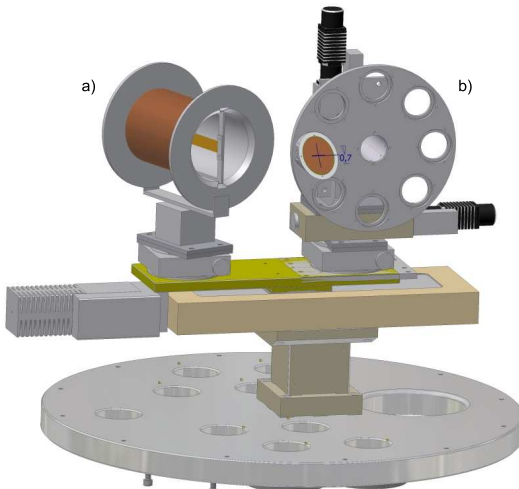


Figure 2.4: The goniometer holds several radiators that can be inserted onto the beam axis (b). Also available is a MØLLER radiator [Wall].

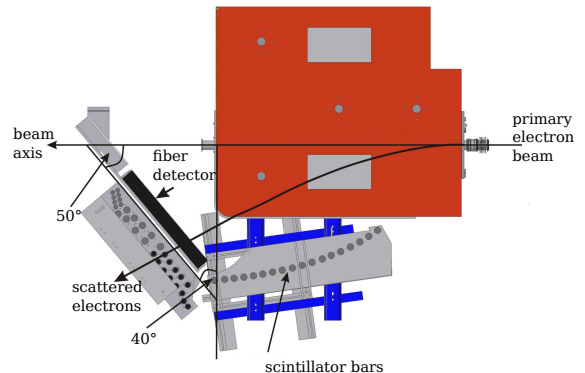


Figure 2.5: Top-down view of the tagging system consisting of dipole magnet (red) and scintillating bars and fibers [For10]. Electrons are deflected by the magnet after the bremsstrahlung process.

2.2 Liquid hydrogen target

The (polarized) photon beam impinges on a liquid hydrogen target [Ham09] which is located at the center of the crystal barrel detector, see Figure 2.1. It consists of a Kapton cell that measures 5.1 cm in length and 3 cm in diameter which is filled with liquid hydrogen. A separate cooling circuit with liquid hydrogen ensures the hydrogen that is used as target material stays liquid. Kapton is chosen as material for the target cell because the expected rate of hadronic reactions induced in the target cell is

¹ Hereby, the recoil energy absorbed by the nuclei is neglected.

² Full Width Half Maximum.

small compared to the expected rate from liquid hydrogen [Ham09]. Protons are bound with a binding energy of 21.4 eV in the target material, which is negligible on the scale of hadronic reaction energies, so that they can be considered free. A schematic view of the target is shown in Figure 2.6.

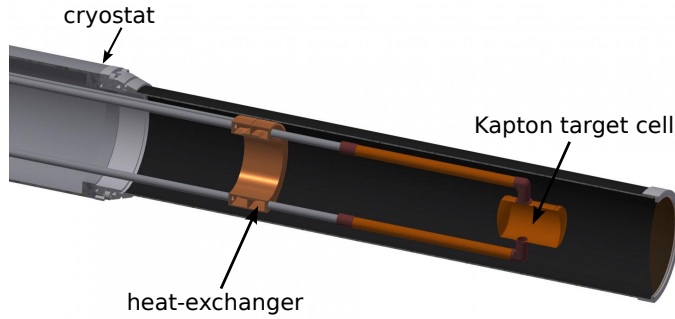


Figure 2.6: Schematic overview of the liquid hydrogen target. Two tubes connected to a heat exchanger and the Kapton cell allow filling it with liquid hydrogen. M. GRÜNER in [Afz19].

2.3 Detector system

Hadronic reactions are induced by the photon beam in the target material. As a consequence resonances are excited that decay under emission of mesons. These mesons subsequently decay to e.g. photons. The main calorimeters of the experiment, the Crystal Barrel that is complemented by the forward detector(2.3.2) and the MiniTAPS calorimeter (2.3.3), cover 95% of the solid angle 4π and are especially suited for the detection of photons. Charged particles are identified by the inner detector (2.3.1) as well as plastic scintillators mounted in front of the forward and the MiniTAPS detector that are used as vetoes. To suppress electromagnetic reactions a ČERENKOV detector is used (2.3.4). The photon flux is measured via the Gamma-Intensity-Monitor (GIM) and Flux-Monitor (FluMo) (2.3.5).

2.3.1 Inner detector

The inner detector [Fös00; Suf+05] encloses the target in a cylindrical geometry and consists of 513 plastic scintillation fibers that are placed in three layers. The outer layer is oriented along the beam axis while the inner layers are tilted by an angle of -24.5° and 25.8° , respectively, see Figure 2.7. This structure allows to determine the azimuthal and polar angle of a charged particle as long as at least two layers are hit. The detector is in total 40 cm long and covers a polar angle range of $23.1^\circ < \theta < 166^\circ$ with a resolution of 0.4° in polar angle θ and 0.1° in azimuthal angle ϕ . The fibers consist of Polystyrene with a refractive index of $n = 1.6$ and are cladded by Polymethylmethacrylat ($C_5H_8O_2$) with $n = 1.49$ [PDG]. Charged particles passing the detector will cause the emission of scintillation light by the Polystyrene molecules which is read out with photomultipliers after passing lightguides. Short decay times ensure a fast time signal and a time resolution of $FWHM = (2.093 \pm 0.013)$ ns is reached [Har08].

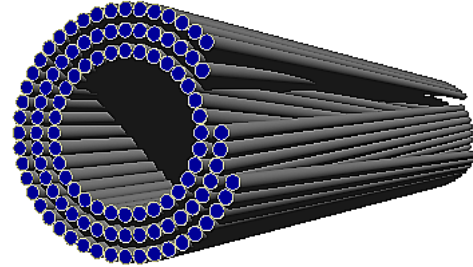


Figure 2.7: The inner detector with three layers of scintillating fibers. The inner two layers are tilted with respect to the outer layer. D. WALTHER in [Afz19].

2.3.2 Crystal Barrel and forward detector

The main calorimeter of the experiment is the Crystal Barrel detector [Ake+92]. It consists of 1320 CsI(Tl) crystals that are arranged in 24 rings facing the center of the target, see Figure 2.8. The first

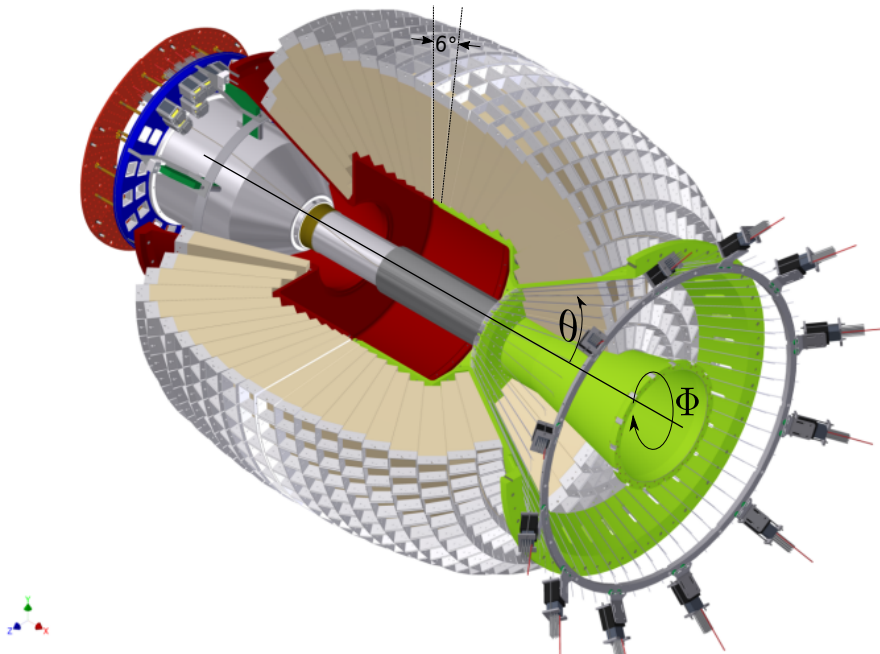


Figure 2.8: Crystal barrel calorimeter and forward detector are built such that they enclose the target and the inner detector. The forward detector consists of the first three rings (green base) of crystals which are additionally covered by plastic scintillators for charged particle identification. The definition of polar angle θ and azimuthal angle ϕ in the LAB system are indicated as well. D. WALTHER in [Urb17]

three rings in forward direction contain 30 crystals each and build the forward detector, covering the polar angle range $11.18^\circ < \theta < 27.54^\circ$. Also the 24th ring contains 30 crystals, all other rings are made up of 60 crystals. The crystals are shaped like truncated trapezoidal pyramids that cover 6° in

polar angle θ and azimuthal angle ϕ . Only in the first three and the last ring the crystals cover 12° in ϕ . Full coverage in ϕ and 80% ($12^\circ < \theta < 156^\circ$) coverage in θ are achieved by the forward detector and the Crystal Barrel. Photons from neutral mesonic decays are very high energetic and will interact with the inorganic scintillator material mainly via pair production [Leo94]. The produced electrons and positrons will themselves interact mainly via bremsstrahlung such that usually an electromagnetic shower is created upon photon impact that may spread over several crystals. Using crystals with a length of $l = 30$ cm photons with an energy of up to 2 GeV may deposit their entire energy in the calorimeter since the l corresponds to 16.22 radiation lengths X_0 [Ake+92]. The transversal spread of a shower is given by the MÓLIERE radius which is 3.8 cm for CsI(Tl) [Ake+92]. By determining the focal point of the electromagnetic showers an angular resolution of less than 2° can be achieved [Jun04] while the energy resolution is given by [Ake+92]

$$\frac{\sigma_E}{E} = \frac{2.5\%}{\sqrt[4]{E/\text{GeV}}}, \quad (2.3)$$

depending on the initial photon energy E . The energy loss of heavier charged particles, e.g. a proton, is described by the BETHE-BLOCH formula [Bet30]. Depending on their mass they only deposit their full energy up to a certain threshold energy above which they are characterized as Minimal Ionizing Particles (MIP).

The emitted scintillation light of crystals not belonging to the forward detector is read out using PIN photodiodes. A wavelength shifter ensures meeting the sensitive spectral range of the photodiodes. The long decay times of the scintillation light and the slow preamplifiers following the photodiodes do not allow the determination of a timing information for particles detected in the Crystal Barrel³, so that the Crystal Barrel is optimized for energy measurements.

Crystals belonging to the forward detector are read out using Photomultipliers. They provide a faster signal, such that timing information for forward detector hits is available with a time resolution of $\text{FWHM} = (1.861 \pm 0.016)$ ns [Har08]. Additionally plastic scintillator plates are mounted in front [Wen04], allowing the identification of charged particles with an efficiency of 72% [Geh15]. Optical fibers guide the scintillation light from the plates to photomultipliers.

2.3.3 MiniTAPS

Since the Crystal Barrel only covers the solid angle starting at $\theta \approx 12^\circ$. It is supplemented by the Mini-Two-Arm-Photon-Spectrometer (MiniTAPS) [Gab+94; Str96] for polar angles $1^\circ < \theta < 12^\circ$. The MiniTAPS detector is placed in a distance of $d = 2.1$ m from the target and consists of 216 hexagonally shaped BaF₂ crystals, see Figure 2.9. Each crystal has a length of $l = 25$ cm which is equivalent to 12 radiation lengths [Nov91] and a width of $w = 5.8$ cm. The chosen material has a high density and is able to withstand high reaction rates [PDG]. This is important here because most reactions will be strongly boosted in forward direction towards small θ . Different mechanisms of scintillation allow to extract a fast and a slow component [Leo94] which are read out using photomultipliers and separately used for timing and energy information, respectively. Hereby a time

³ As of 2014, the PIN photodiodes have been replaced by avalanche photodiodes (APD) [Hon14; Urb17], allowing a fast read out that can be used to provide timing information and also as part of the trigger.

resolution of $\text{FWHM} = (0.872 \pm 0.006)$ ns [Har08] and an energy resolution of [Gab+94]

$$\frac{\sigma_E}{E} = 1.9\% + 0.59\% \cdot \sqrt{E/\text{GeV}} \quad (2.4)$$

is achieved. At the same time an angular precision of 0.2° in θ is reached.

In front of each BaF_2 crystal, plastic scintillator plates are mounted to identify charged particles. Their scintillation light is guided towards photomultipliers using optical fibers. With these scintillators a time resolution of $\text{FWHM} = (3.06 \pm 0.05)$ ns is obtained [Har08].

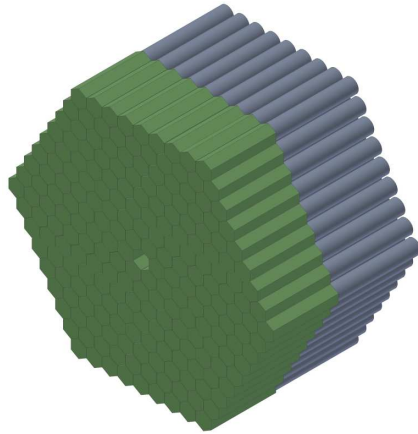


Figure 2.9: The MiniTAPS detector is made up of 216 BaF_2 crystals (grey). In front of each crystal, plastic scintillators are mounted for charged particle information. Taken from [Wal].

2.3.4 ČERENKOV detector

When the photon beam impinges on the proton target, not only hadronic reactions are induced but also electromagnetic reactions. Because the beam energy is very high on the scale of electromagnetic interactions, any produced electrons and positrons are highly relativistic and boosted to small polar angles. To suppress these events already during data acquisition a ČERENKOV detector [Kai07] is positioned between the MiniTAPS calorimeter and the Crystal Barrel, see Figure 2.1. It is filled with CO_2 gas where ČERENKOV light is emitted by electrons or positrons above an energy of 17.4 MeV. This follows from the refractive index which is given as $n_{\text{CO}_2} = 1.00045$ [PDG]. The emitted ČERENKOV radiation is focused on a photodiode using a parabolic mirror. The presence of a signal can then be used as veto during data acquisition to reduce the amount of recorded electromagnetic background. Electrons and positrons are detected with an efficiency of up to $(99.72 \pm 0.45)\%$ [Kai07].

2.3.5 Flux monitoring

The FluMo and GIM detector are used to determine the total number of photons incident on the target and are located behind the MiniTAPS detector, as is shown in Figure 2.1.

The GIM detector [McG08] is made of 16 PbF_2 crystals placed in a 4×4 array, see Figure 2.10. Incoming photons will interact with the material mainly via pair production [Leo94]. The produced electrons and positrons are highly relativistic and will emit ČERENKOV light that is collected

with photomultipliers. For reaction rates higher than 5 MHz the GIM detector efficiency decreases significantly. For rates above 7 MHz more than 10% of events are not registered [Har08]. To

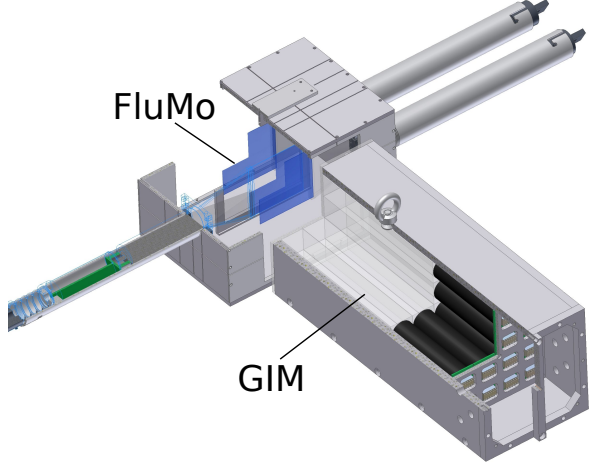


Figure 2.10: The two detectors FluMo and GIM are used to monitor the photon flux at different reaction rates. D. WALTHE in [Afz19].

compensate this the FluMo detector [Die08] is used as soon as deadtime effects influence the performance of the GIM detector. A converter plate made of lead, two scintillators and a veto detector are part of the FluMo detector. Impinging photons may create electron positron pairs that are detected in a coincidence measurement using the two scintillators. A plastic scintillation detector is placed before the converter plate and gives a veto signal if charged particles pass through it.

2.4 Trigger

To minimize the volume of data that is saved to disk for offline analysis, data is only digitized if certain predefined patterns in the detector signals are present. The search for predefined patterns is managed by the trigger of the experiment. The analyzed data sets were acquired using the *vme_trig42c* trigger [Win06; Hof18]. The trigger requires configuration to be sensitive to hadronic photoproduction reactions and at the same time reject unwanted background events. This is achieved using Field Programmable Gate Arrays (FPGAs) which allows to split the trigger into two levels: At first level all detectors with a fast read out system (up to 250 ns) are checked for hits. At the second level the number of detected particles in the Crystal Barrel is determined using the Fast Cluster Encoder (FACE), which can take up to 10 μs [Fle01]. It is always demanded that at least two particles are measured in either forward, MiniTAPS or Crystal Barrel detector while no veto from the ČERENKOV detector is measured. Any information from the Crystal Barrel is only available in the second level because of the slow readout.

2.5 Software and Monte Carlo

In order to proceed with the offline data analysis of CBELSA/TAPS, several software tools are used that are described briefly in the following.

2.5.1 ExPLORA

Within the CBELSA/TAPS collaboration an analysis software has been developed named *Extended Pluggable Object-oriented Root Analysis (ExPLORA)* [Sch+]. It is based on *ROOT* [BR97] and is used for reconstruction and analysis of acquired raw data. *ROOT* has been developed at CERN to deal with a high amount of data. It makes use of *C++* libraries that give it high functionality regarding statistical analyses, visualizations and data management. *ExPLORA* is also written in *C++* but is operated by the use of *xml* files. This allows user specific extensions in the form of plugins that manage e.g. the application of cuts and the filling of histograms. In order to select candidates for the reaction $\gamma p \rightarrow p\eta' \rightarrow p\gamma\gamma$ a *C++* plugin has been written that was embedded into a *xml* file which managed the application of calibrations and reconstruction. For further analysis of the selected data, scripts in *ROOT* and *python* have been written. In Appendix A an example *.xml* file is displayed.

2.5.2 Monte Carlo

In order to determine detector and analysis acceptances as well as possible background contributions it is convenient to simulate the according detector geometry and the interaction of particles with the material using the Monte Carlo technique [MU49]. Based on the CERN-developed software package *Geant3* (Geometry and Tracking) [Bru+87] a simulation of the CBELSA/TAPS experiment was developed using the Virtual Monte Carlo technique [Kal11]. Hereby the particles' interaction with the detector materials are modeled according to existing experimental data. Simulated datasets may then be analyzed in the same way as measured data in order to check consistency with the measured data as well as investigating detection efficiencies and background contributions. Table 3.2 shows the simulated datasets that were used during the analysis and how many events were generated for each reaction, respectively. The reactions $\gamma p \rightarrow p2\pi^0 \rightarrow p4\gamma$ $\gamma p \rightarrow p\pi^0\eta \rightarrow p4\gamma$ proved to be responsible for background contamination after the event selection (see Chapter 3). These reactions were simulated while additionally weighting all events according to the production cross section determined from a BnGa fit [AKN+; Ani+12]. These Monte Carols were kindly provided by P. MAHLBERG [Mah22].

Reaction	Number of events
$\gamma p \rightarrow p\pi^0$	$60 \cdot 10^6$
$\gamma p \rightarrow p\eta$	$30 \cdot 10^6$
$\gamma p \rightarrow p\omega \rightarrow p\pi^0\gamma$	$30 \cdot 10^6$
$\gamma p \rightarrow p\eta' \rightarrow p\gamma\gamma$	$30 \cdot 10^6$
$\gamma p \rightarrow p2\pi^0$	$60 \cdot 10^6$
$\gamma p \rightarrow p\pi^0\eta$	$60 \cdot 10^6$
$\gamma p \rightarrow p3\pi^0$	$30 \cdot 10^6$
$\gamma p \rightarrow p2\pi^0\eta$	$30 \cdot 10^6$
$\gamma p \rightarrow n\pi^+$	$30 \cdot 10^6$
$\gamma p \rightarrow p\pi^+\pi^-$	$30 \cdot 10^6$

2.5.3 Stan

All BAYESIAN fits that are presented in this thesis are performed using the programming language *Stan* [Sta22]. *Stan* is highly functional for statistical modeling and high-performance statistical computation. Full BAYESIAN statistical inferences can be made with MCMC sampling as well as approximate BAYESIAN inference with variational inference and penalized maximum likelihood estimation with optimization [Sta22]. Stan is written in C++ and can thus handle a large amount of data very efficiently. Interfaces for different data analysis languages are available. In this thesis, the *Python* [RP22] front-end of *Stan*, called *CmdStanPy* was used. Hereby, the model is specified in a `.stan` file which is read and compiled from *Python*. All sampling statements and results can then be accessed directly from *Python*, e.g. using the package *pandas* [McK10]. Appendix A shows an example of a `.stan` file that can be used for the simple example of a linear fit.

2.6 Datasets

The data that was analyzed in the course of this thesis was taken in the period of July 2013 to October 2013. Unpolarized electrons from ELSA were incident on a diamond radiator with 500 μm thickness with a beam energy of $E_0 = 3.2 \text{ GeV}$ and a beam current of roughly 1 nA. Thus, linearly polarized photons were created that impinged on a liquid hydrogen target. All beam times used the *vme_trig42c* that has been described previously.

The coherent edge position was chosen at 1750 MeV for the July and August beam times and at 1850 MeV for the September and October beam times, enabling an analysis of the beam asymmetry Σ in the beam energy range from $E_\gamma \approx 1100 \text{ MeV}$ to 1800 MeV . 4919 runs were taken in total with alternating radiator orientation $\alpha^{\parallel/\perp} = 45^\circ$, see Figure 4.1. The photon beam polarization was determined as part of the work [Afz19] using ANB calculations, as described in Section 2.1. Table 2.1 shows a summary of the key parameters of the 2013 beam time taken at the CBELSA/TAPS experiment.

beamtime	number of runs (h)	coherent edge position
July 2013	513 (111)	1750 MeV
August 2013	1832 (396)	1750 MeV
September 2013	1490 (323)	1850 MeV
October 2013	1084 (235)	1850 MeV

Table 2.1: Summary of the key parameters of the 2013 beam time at CBELSA/TAPS taken for the measurement of the beam asymmetry Σ . Taken from [Afz19].

APPENDIX A

Illustration of used software tools

A.1 ExPLORA

Figure A.1 shows an example of a .xml file that was used to call the plugin that was written to select the reaction $\gamma p \rightarrow p\eta' \rightarrow p\gamma\gamma$. First of all, several files have to be included in order to acquire certain *containers* that inhibit the raw data of the final state particles. Then the plugin is embedded with the options

- MC (bool) – determines whether Monte Carlo or measured data are analyzed
- PWA (bool) – determines whether used Monte Carlo simulation have PWA weights
- FOURGAMMAS (bool) – determines whether the generated final state has four photons or two
- REALGAMMAS (bool) – determines whether real photons are part of the decay or not (e.g. $n\pi^+$)
- allroutes (CBTConfigString) – gives the container that contains the routes of charged particles

```
1  <explora>
2    <!-- Flags can be set and later on used (e.g. as conditions) -->
3    <CBTFlag name="CONFIGS" value="/hadron/krause/git/exploraConfigs"/>
4    <CBTIncludeXML file="${CONFIGS}/Analyse/DataSource/RawData_Prefiltered.xml"/>
5    <!-- Merges particles from different sources in a common container -->
6    <CBTParticleMerger source="CBGammmas,MiniTapsGammmas" container="allgammmas" persistent="no" />
7
8    <!-- = Selection plugins ===== -->
9    <!-- Now you have all the particle containers and can start to select events. The analysis of preselected data starts here... -->
10   <CBTIncludeXML file="${CONFIGS}/ReactionSelection/Proton23PED.xml" />
11   <!--This is for 2.5PED events -->
12   <CBTRouteGammaFactory srccontainer="chapirooutes" dstcontainer="chapiroutegammmas"/>
13   <CBTRouteGammaFactory srccontainer="FWPlugVetoRoutes" dstcontainer="fproutegammmas"/>
14   <CBTRouteGammaFactory srccontainer="MiniTapsVetoRoutes" dstcontainer="minitapsroutegammmas"/>
15   <CBTParticleMerger source="chapiroutegammmas, fproutegammmas, minitapsroutegammmas" container="allroutes"/>
16   <!-- = Histogramming ===== -->
17   <!-- The histogrammer creates and fills all the histograms which should be stored in your output file -->
18   <CBTHistogrammer profile="yes" profilehisto="yes">
19     <!--here the written plugin is called -->
20     <CBTetaprimeanalysis MC="FALSE" PWA="FALSE" FOURGAMMAS="FALSE" REALGAMMAS="TRUE" allroutes="allroutes"/>
21   </CBTHistogrammer>
22 </explora>
```

Figure A.1: Example .xml file that was used to call the plugin CBTetaprimeanalysis.cpp (line 20) with several self defined options.

A.2 Stan

The simplest regression that can be made with *Stan* is of the form

$$y = a \cdot x + b + \epsilon. \quad (\text{A.1})$$

Here y is a measured quantity with GAUSSIAN noise ϵ , x are predictors and a and b are slope and intercept of a linear regression. Assuming each datapoint y_n is independent and exhibits an individual noise term $\epsilon_n \sim \mathcal{N}(0, \sigma_n)$, the likelihood $p(y|a, b)$ can be formulated as

$$y_n \sim \mathcal{N}(a \cdot x_n + b, \sigma_n) \quad \Leftrightarrow \quad p(y|a, b) = \prod_{i=1}^N \mathcal{N}(y_i|a \cdot x_i + b, \sigma_i), \quad (\text{A.2})$$

if there are N datapoints in total. Specifying e.g. normal priors for the two regression coefficients a and b completes the inference

$$a \sim \mathcal{N}(0, 1) \quad b \sim \mathcal{N}(0, 1). \quad (\text{A.3})$$

Figure A.2 shows the implementation of the described model in *Stan*. First of all, all data that is read in has to be defined. Conveniently this can be done using the `vector` class, that corresponds to a list of e.g. all x values. Next, the parameters of the model are defined and lastly the likelihood and priors are specified.

```

1  data {
2    int<lower=0> n; //number of datapoints
3    vector[n] x; //predictors
4    vector[n] y; //measured quantity
5    vector[n] y_err; //measurement error
6  }
7  parameters {
8    real a;
9    real b;
10 }
11 model {
12   //likelihood
13   y ~ normal(a*x+b, y_err);
14   //priors
15   a ~ normal(0,1);
16   b ~ normal(0,1);
17 }
```

Figure A.2: Example .stan file that can be used to perform a simple linear fit.

APPENDIX B

Additional plots and calculations

This chapter will give additional calculations and plots which would have interrupted the train of thought unnecessarily in the main part.

B.1 Statistical error for the asymmetry $A(\phi)$

Let $\tilde{N}_i^{\parallel/\perp}$ be the normalized event yields at bin ϕ_i . As mentioned in section 4.1, the asymmetry A_i at bin i is then given by

$$A_i = \frac{\tilde{N}_i^\perp - \tilde{N}_i^\parallel}{p_\gamma^\parallel \tilde{N}_i^\perp + p_\gamma^\perp \tilde{N}_i^\parallel} = \Sigma \cos(2(\alpha^\parallel - \phi_i)), \quad (\text{B.1})$$

where the event yields are normalized over all M ϕ -bins

$$\tilde{N}_i^{\parallel/\perp} = \frac{N_i^{\parallel/\perp}}{\sum_{j=1}^M N_j^{\parallel/\perp}}.$$

To estimate statistical errors according to GAUSSIAN error propagation, the partial derivatives with respect to $\tilde{N}_i^{\parallel/\perp}$ have to be built:

$$(\Delta A_i)^2 = \left(\frac{\partial A_i}{\partial \tilde{N}_i^\parallel} \Delta \tilde{N}_i^\parallel \right)^2 + \left(\frac{\partial A_i}{\partial \tilde{N}_i^\perp} \Delta \tilde{N}_i^\perp \right)^2, \quad (\text{B.2})$$

where

$$\left(\frac{\partial A_i}{\partial \tilde{N}_i^{\parallel/\perp}} \right)^2 = \left[\frac{\tilde{N}_i^{\perp/\parallel} (p_\gamma^\perp + p_\gamma^\parallel)}{(p_\gamma^\parallel \tilde{N}_i^\perp + p_\gamma^\perp \tilde{N}_i^\parallel)^2} \right]^2, \quad (\text{B.3})$$

$$\text{and with } \tilde{N}_i^{\perp/\parallel} = \tilde{N}_i \quad (\text{B.4})$$

$$(\Delta \tilde{N}_i)^2 = \left[\frac{\partial}{\partial N_i} \left(\frac{N_i}{\sum_j N_j} \right) \cdot \Delta N_i \right]^2 + \sum_{j \neq i} \left[\frac{\partial}{\partial N_j} \left(\frac{N_i}{\sum_j N_j} \right) \cdot \Delta N_j \right]^2 \quad (\text{B.5})$$

$$= \left[\frac{\sum_{j \neq i} N_j}{\left(\sum_j N_j \right)^2} \cdot \Delta N_i \right]^2 + \sum_{j \neq i} \left[-1 \cdot \frac{N_i}{\left(\sum_j N_j \right)^2} \cdot \Delta N_j \right]^2 \quad (\text{B.6})$$

$$= \frac{1}{\left(\sum_j N_j \right)^4} \cdot \left[\left(\sum_{j \neq i} N_j \cdot \Delta N_i \right)^2 + \sum_{j \neq i} \left(N_i \cdot \Delta N_j \right)^2 \right]. \quad (\text{B.7})$$

One can then further use that $(\Delta N_i)^2 \approx N_i$. This holds only approximately, since the histograms are filled N times with weights w_n (see chapter 3.3), but since the weights are either $w = 1$ or $w \ll 1$

$$\Delta N_i = \sqrt{\sum_{n=1}^N w^2} \approx \sqrt{N_i}. \quad (\text{B.8})$$

B.2 Kinematic variables for each bin

B.2.1 Coplanarity

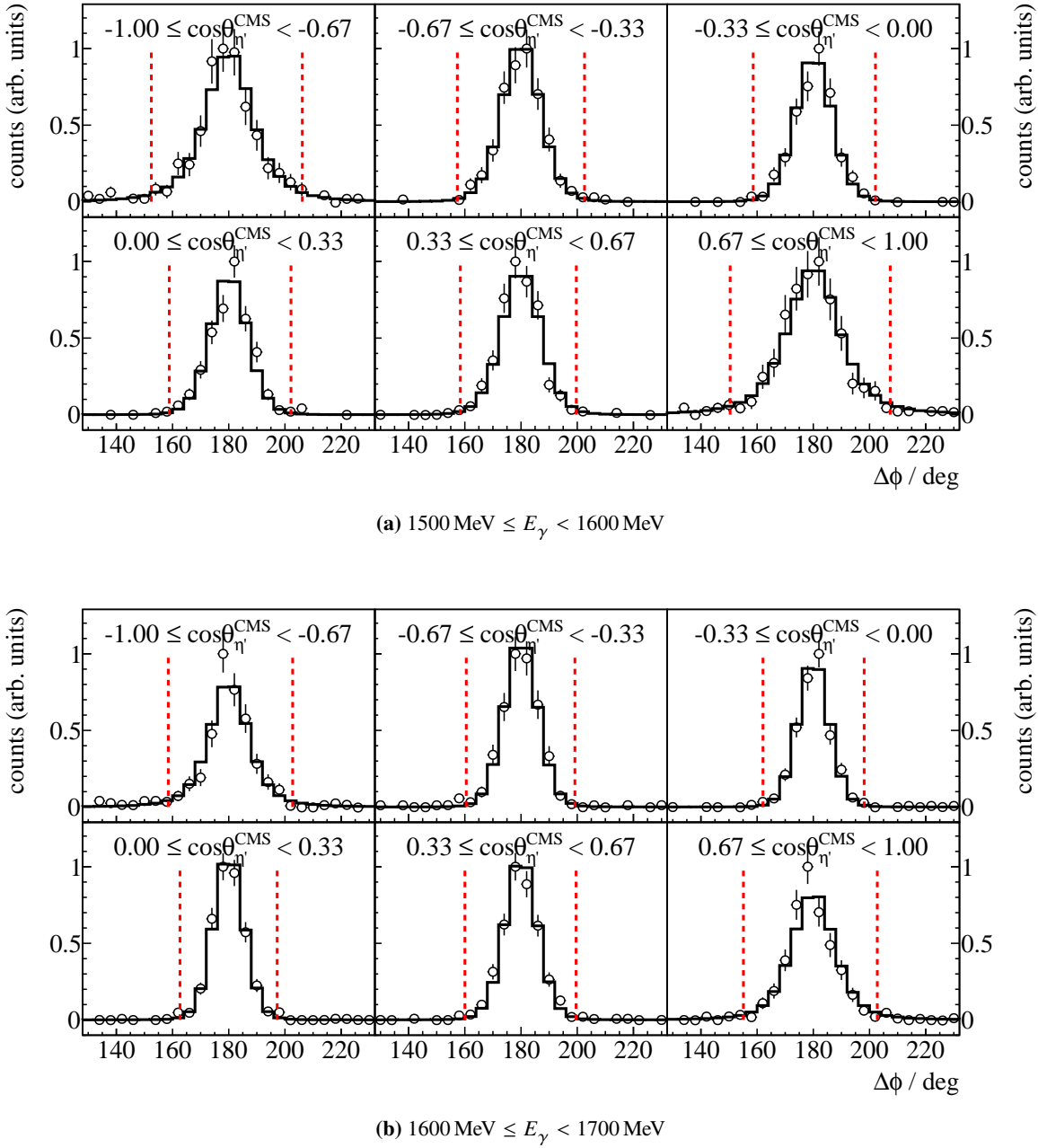


Figure B.1: Coplanarity $\Delta\phi$ for all energy and angular bins. Data points are displayed as open circles, scaled Monte Carlo data belonging to η' photoproduction is displayed as solid histogram. The determined cut ranges are indicated by the dashed red lines.

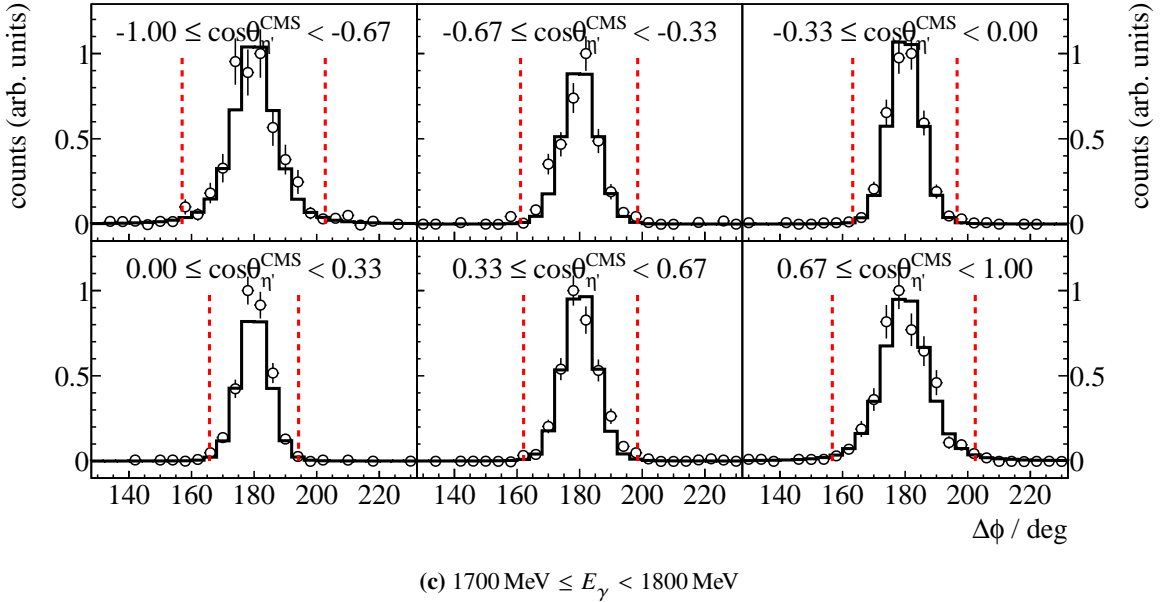


Figure B.1: Coplanarity $\Delta\phi$ for all energy and angular bins. Data points are displayed as open circles, scaled Monte Carlo data belonging to η' photoproduction is displayed as solid histogram. The determined cut ranges are indicated by the dashed red lines.

Figure B.1 shows the coplanarity for all energy and angular bins. Cut ranges were determined from a GAUSSIAN fit to the data points. Only slight dependency on beam energy and meson polar angle can be identified. Only η' Monte Carlo data are fitted because the measured points do not give enough reference points for the fit to identify different contributing final states. There is good agreement between Monte Carlo simulations and measured data.

B.2.2 Polar angle difference

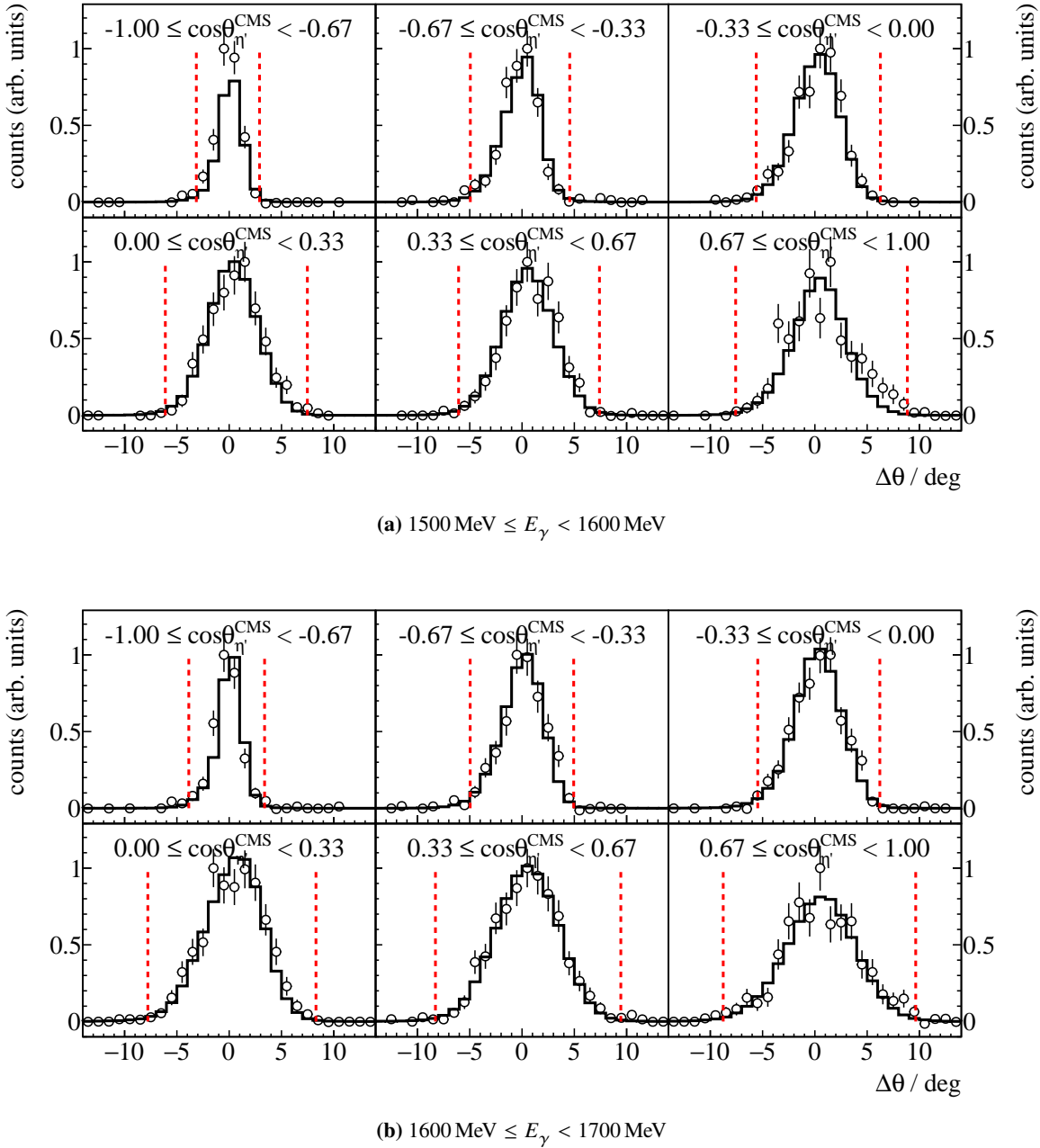


Figure B.2: Polar angle difference $\Delta\theta$ for all energy and angular bins. Data points are displayed as open circles, scaled Monte Carlo data belonging to η' photoproduction is displayed as solid histogram. The determined cut ranges are indicated by the dashed red lines.

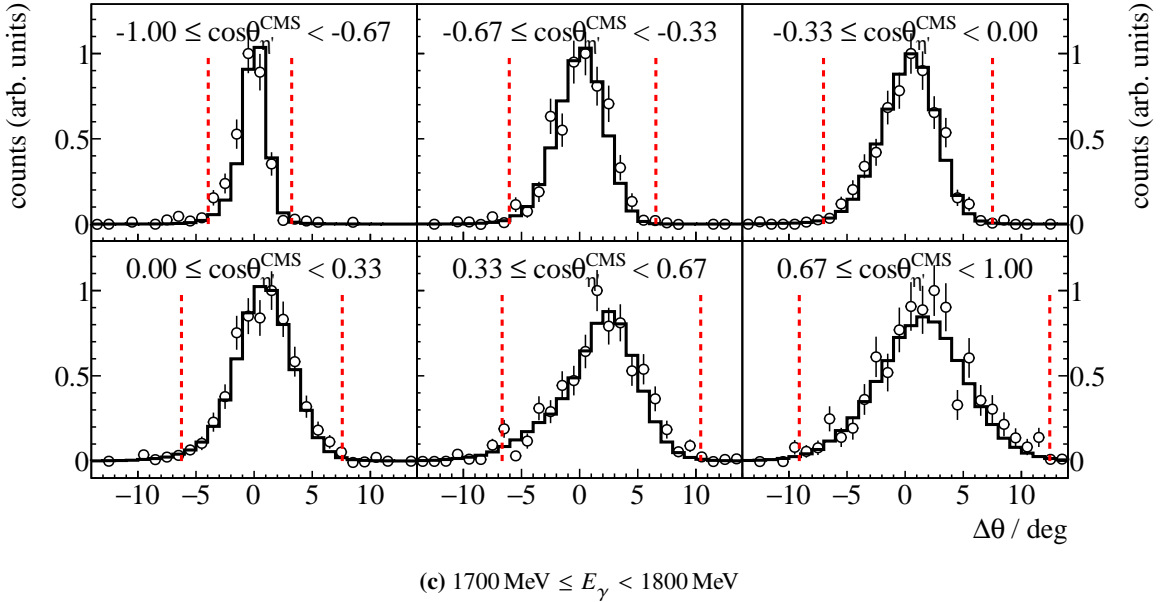


Figure B.2: Polar angle difference $\Delta\theta$ for all energy and angular bins. Data points are displayed as open circles, scaled Monte Carlo data belonging to η' photoproduction is displayed as solid histogram. The determined cut ranges are indicated by the dashed red lines.

Figure B.2 shows the polar angle difference for all energy and angular bins. Cut ranges were determined from a GAUSSIAN fit to the data points. Only slight dependency on beam energy can be identified whereas clear correlation between width of the distribution and meson polar angle exists. This is due to the hit detectors which exhibit different angular resolutions, as has been discussed in the main part. Only η' Monte Carlo data are fitted because the measured points do not give enough reference points for the fit to identify different contributing final states. There is good agreement between Monte Carlo simulations and measured data.

B.2.3 Missing mass

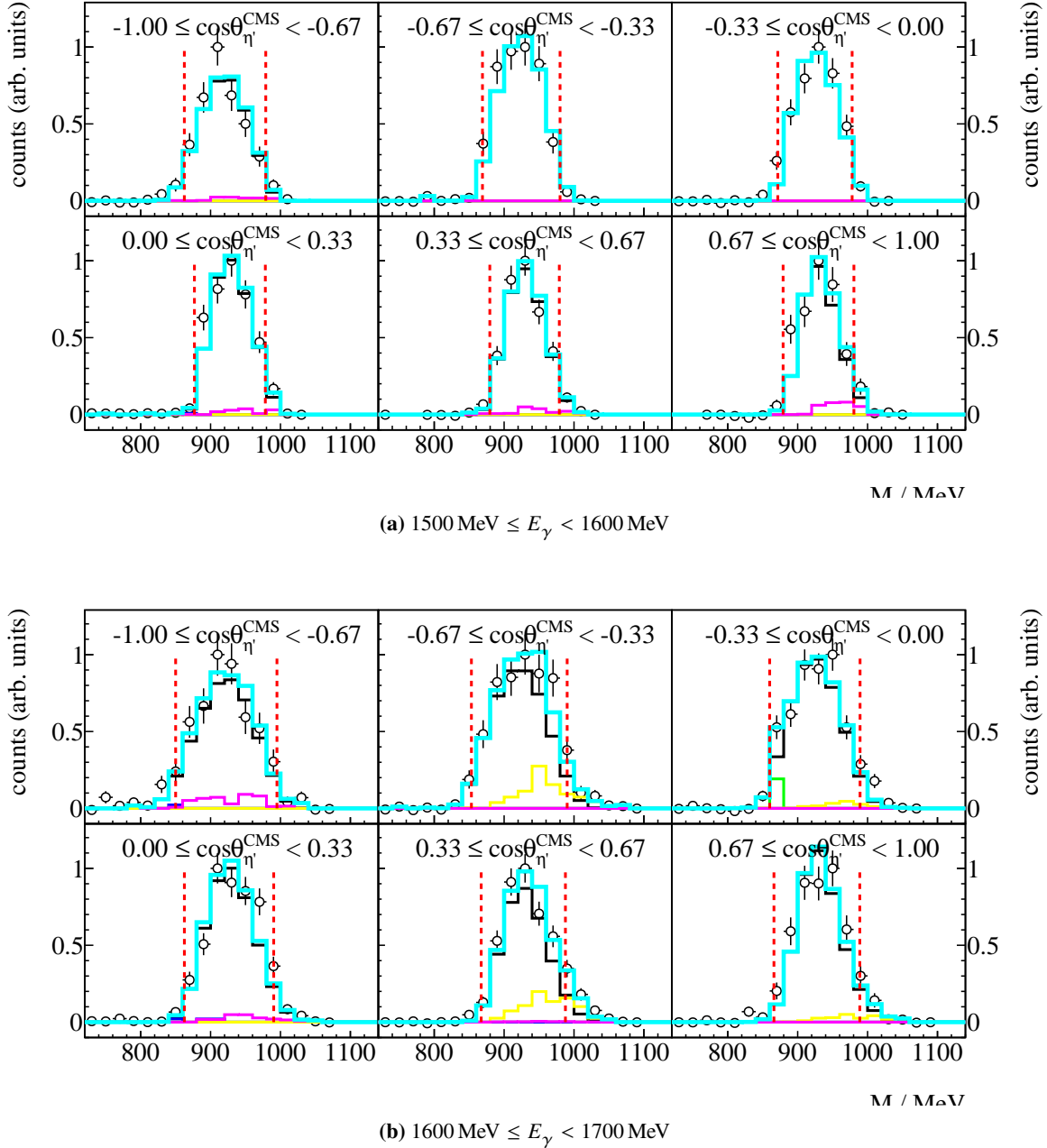


Figure B.3: Missing mass m_x for all energy and angular bins. Data points are displayed as open circles, scaled Monte Carlo data belonging to η' (black), $2\pi^0$ (yellow) and $\pi^0\eta$ (magenta) photoproduction is displayed as solid histogram while their sum is displayed as turquoise histogram. The determined cut ranges are indicated by the dashed red lines.

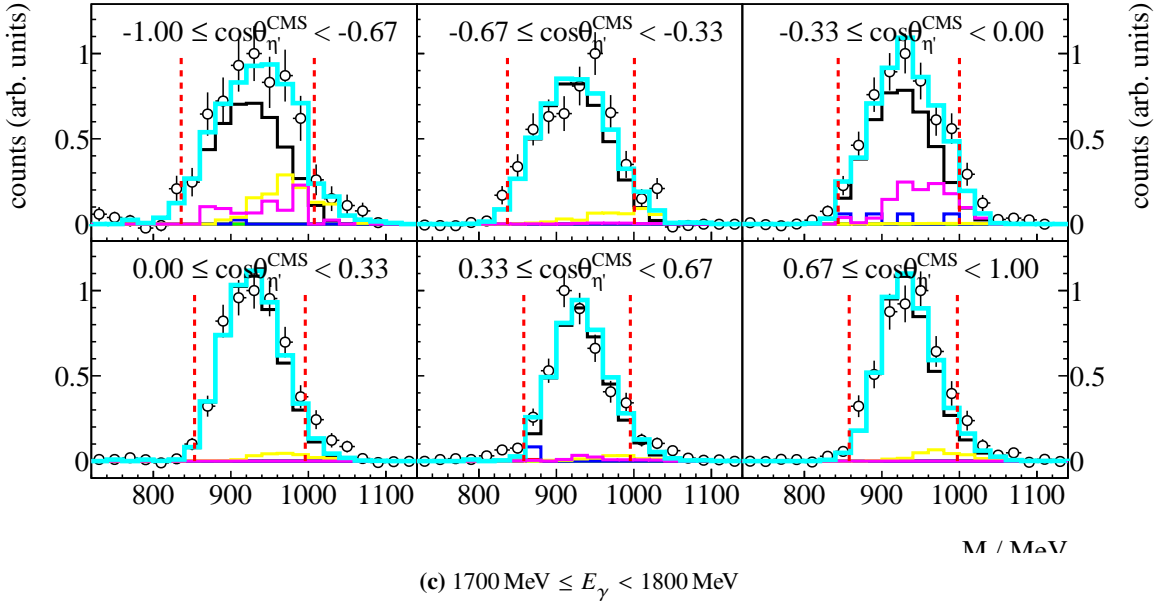


Figure B.3: Missing mass m_X for all energy and angular bins. Data points are displayed as open circles, scaled Monte Carlo data belonging to η' (black), $2\pi^0$ (yellow) and $\pi^0\eta$ (magenta) photoproduction is displayed as solid histogram while their sum is displayed as turquoise histogram. The determined cut ranges are indicated by the dashed red lines.

Figure B.3 shows the missing mass for all energy and angular bins. Cut ranges were determined from a Novosibirsk fit to the Monte Carlo data. Only slight dependency on meson polar angle can be identified. Especially at higher beam energies the missing mass peak grows wider with flat background contributions from $2\pi^0$ and $\pi^0\eta$ production towards higher masses. The Monte Carlo fit mostly shows consistency with the fit of the invariant mass spectra. However, spectra are to be seen with caution, since the shapes of the two different background contributions are very similar and there is no other reference point in the missing mass spectrum as opposed to the invariant mass. Fits to the invariant mass spectra may reveal background contributions where a fit to the missing mass spectrum failed to find any. There is good agreement between Monte Carlo simulations and measured data.

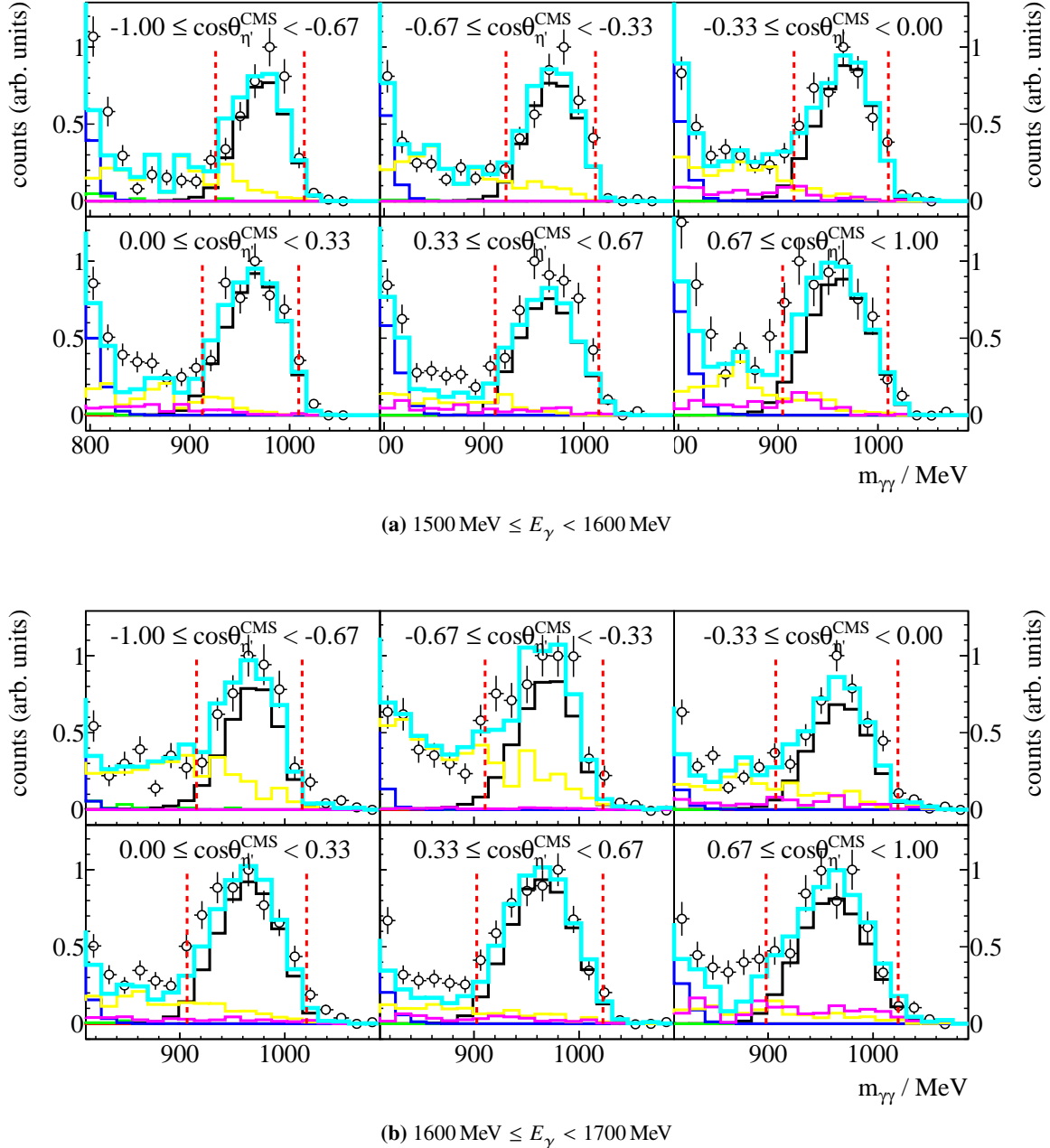
B.2.4 Invariant mass


Figure B.4: Invariant mass m_{meson} for all energy and angular bins. Data points are displayed as open circles, scaled Monte Carlo data belonging to η' (black), $2\pi^0$ (yellow), $\pi^0\eta$ (magenta), π^0 (green) and ω (blue) photoproduction is displayed as solid histogram while their sum is displayed as turquoise histogram. The determined cut ranges are indicated by the dashed red lines.

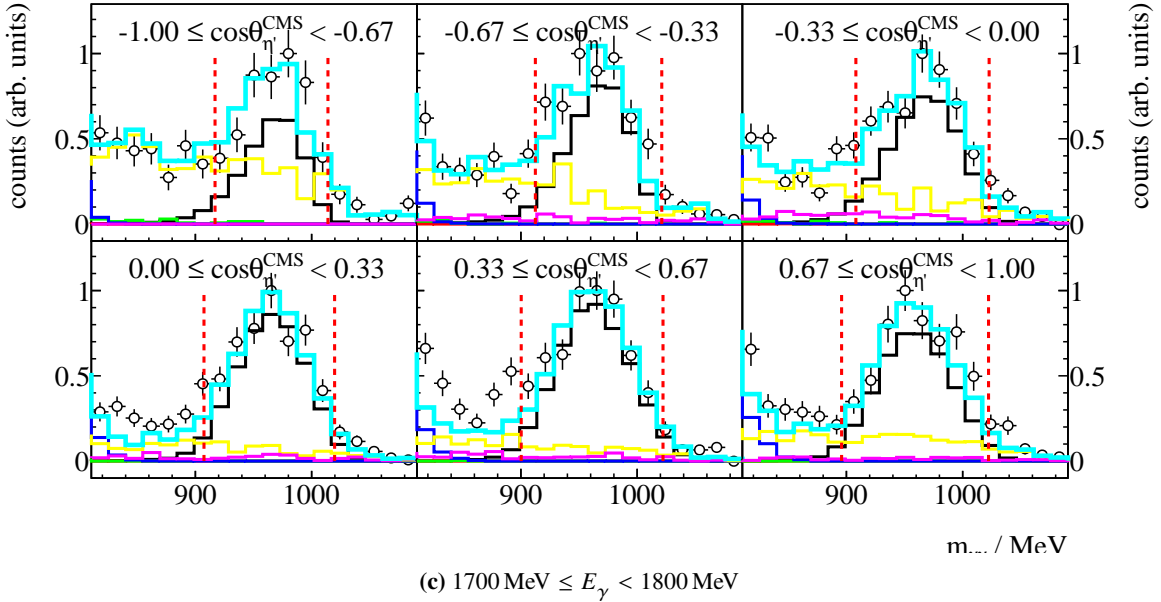


Figure B.4: Invariant mass m_{meson} for all energy and angular bins. Data points are displayed as open circles, scaled Monte Carlo data belonging to η' (black), $2\pi^0$ (yellow), $\pi^0\eta$ (magenta), π^0 (green) and ω (blue) photoproduction is displayed as solid histogram while their sum is displayed as turquoise histogram. The determined cut ranges are indicated by the dashed red lines.

Figure B.4 shows the invariant mass for all kinematic bins. Hardly any dependence on meson direction and beam energy is observed. However, background contributions are especially observed in very forward and backward direction towards higher beam energies in consistency with findings from the missing mass spectra. A flat background is realized by $2\pi^0$ and $\pi^0\eta$ production. There is good agreement between Monte Carlo simulations and measured data.

APPENDIX C

Discussion of binned fits

Investigation of toy Monte Carlo experiments (cf. section 4.3) revealed that the choice of binning leads to systematic errors regarding the parameter Σ when fitting a binned distribution to the equation

$$A(\phi) = \Sigma \cdot \cos(2(\alpha^{\parallel} - \phi)). \quad (\text{C.1})$$

To investigate this further, the distributions $A(\phi)$ from different toy Monte Carlo experiments where fitted for several binnings in ϕ . Three different Monte Carlo experiments were considered, each corresponding roughly to the expected statistics in one kinematic bin for π^0 , η and η' photoproduction, respectively. For simplicity's sake, only least squares fits are shown here, although similar results were found for BAYESIAN fits also. The equivalency of BAYESIAN and least squares fit has been demonstrated sufficiently up until now. To identify the bias that is introduced by binning the data, 10000 toy Monte Carlo bins for each setting are fitted for $n = 10, 15, 20, \dots, 100$ bins. Then the dependence from the amount of bins of the mean μ of the normalized residuals ξ as well as the mean χ^2 value of all fits is investigated. This is shown in Figure C.1; The fitted mean of the normalized posteriors ξ is plotted against the number of bins (blue data points, left ordinate) as well as the mean χ^2 of 10000 fits depending on the number of bins (red data points, right ordinate). Clear dependencies can be made out: while too few bins tend to underestimate the true value of the beam asymmetry, too much bins will lead to an overcompensation. For this reason, the functions $\chi^2(n)$ and $\mu(n)$ are monotonously rising with increasing number of bins n . An exception is realized by the samples that simulated the statistics of the η' final state, which can be explained by the fact, that after reaching a certain number of bins, no sensible fit estimates can be made anymore because too few data points are available. A minimum deviation from the nominal value is reached with $n = 10, 20, 30$ bins for statistics comparable to η' , η and π^0 production respectively. This does not coincide with a minimum χ^2 necessarily, although the mean χ^2 values associated with the best estimation of the input value are compatible with 1. Figure C.1 however remarkably shows the influence binning has on the extraction of the beam asymmetry. Since there exist other methods, binned fits should only be used as a sanity check, but generally avoided, to circumvent the introduction of any systematics inherent to binning.

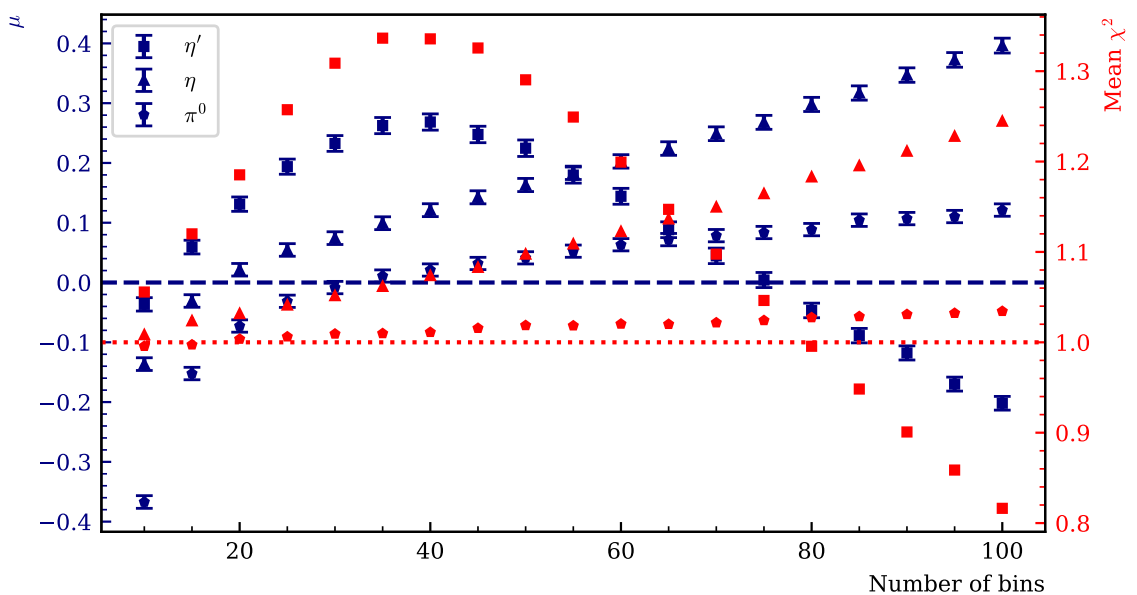


Figure C.1: Fit performance in dependence of the number of bins. Left axis shows the mean μ of the distribution of the normalized residuals ξ , right axis shows the mean χ^2 of all fits. Squares simulate fits with statistics similar to the $\gamma p \rightarrow p\eta' \rightarrow p\gamma\gamma$ final state, triangles statistics similar to the $\gamma p \rightarrow p\eta \rightarrow p\gamma\gamma$ final state, pentagons statistics similar to the $\gamma p \rightarrow p\pi^0 \rightarrow p\gamma\gamma$. Dotted red line indicates the ideal value of $\chi^2 = 1$, while the dashed blue line indicates the ideal mean of the normalized residuals at $\mu = 0$.

APPENDIX D

Investigation of posteriors without truncation

In section 4.3 the investigation of posterior distributions from unbinned BAYESIAN fits was incomplete, since the normalized residuals as well as the likelihood pool could not be built with truncated posteriors. This is now supplemented here. After the fits have been repeated without implementing a truncation for the posteriors, all introduced measures to argue good fit quality can be examined. As a reminder, the data were generated with $\Sigma_1 = 0.5$ and $\Sigma_t = -0.5$. Figure D.1 shows the combined posteriors of all fits. The left hand side shows the normalized residuals Ξ and the right hand side the unnormalized combination of all posteriors. The results completely meet the expectations, the input values for the beam asymmetries are very well reproduced, and the normalized residuals follow a standard normal distribution as GAUSSIAN fits show. Together with the results obtained from the independent likelihood pool (Figure D.2), which is able to reproduce the input values within 1σ , this suffices to conclude correct estimation of distribution widths with no inherent bias, as had already been found in section 4.2.3.

Remark: It turned out that without the amount of statistics that was used in section 4.2, normal priors centered at 0 for the asymmetries Σ_t and Σ will mislead the fit results for these parameters towards 0 if no lower and upper boundaries are used. Instead the priors were then chosen to be uniform on the interval $[-2, 2]$. This imposes boundaries, but will not truncate the posteriors because the distributions are not expected to be this wide. All distributions shown here are generated using this model to complete the full investigation of posteriors. Previous toy Monte Carlo experiments (Figure 4.19) as well as very good agreement between point estimates and posterior distributions (Figure 4.23) together with the results shown here confirm the validity of the fit used in the main part.

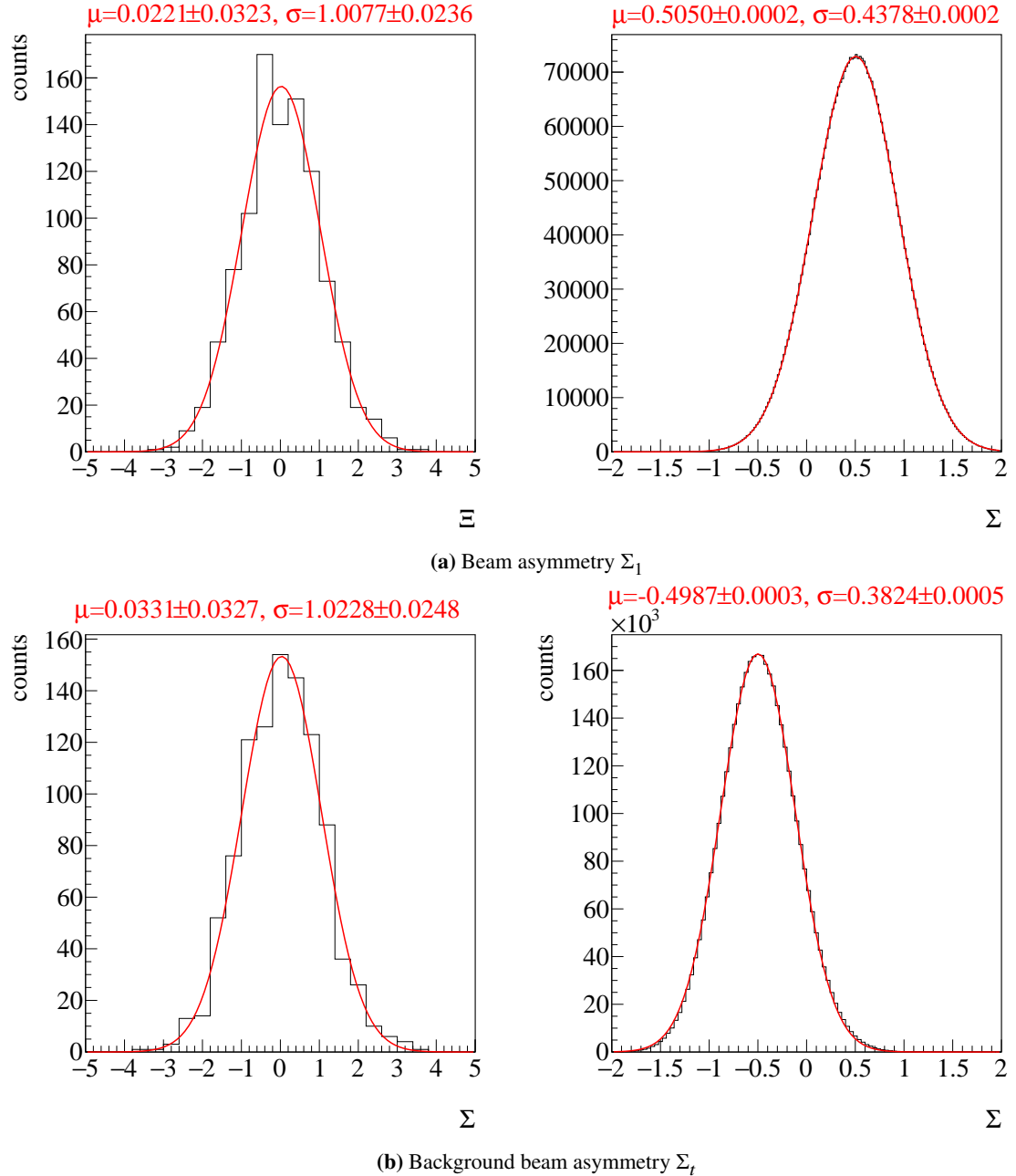


Figure D.1: Combined posteriors of all 1000 fits without truncation for the signal beam asymmetry Σ_1 and the background beam asymmetry Σ_r . Left: normalized residuals Ξ , Right: unaltered added posterior distributions. GAUSSIAN fits have been performed with results given on top of each plot.

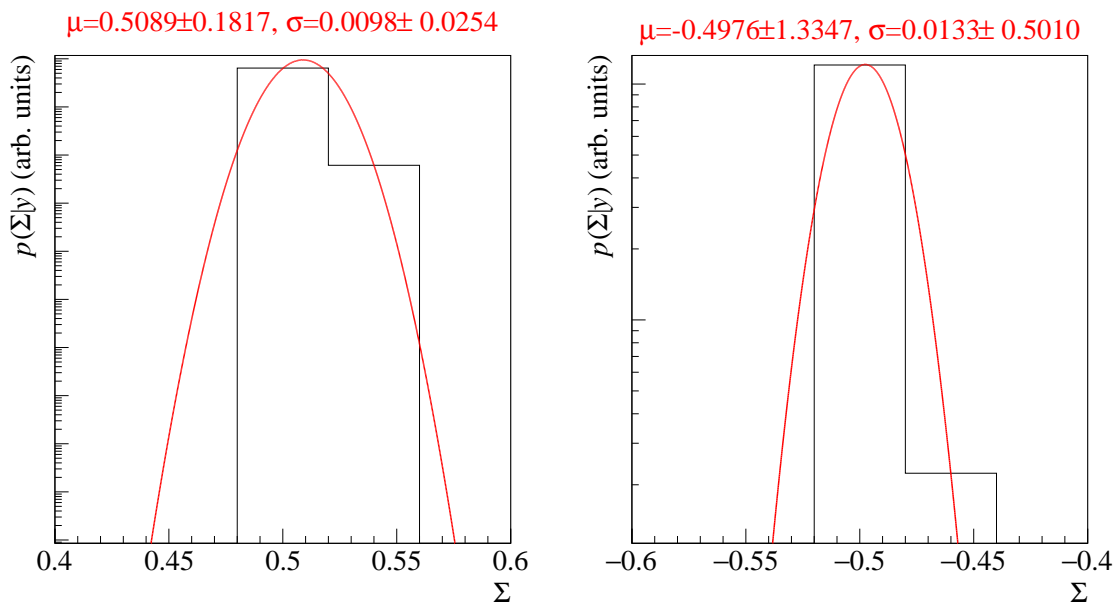


Figure D.2: Posterior distributions of Σ_l (left) and Σ_t (right) combined in an independent likelihood pool. GAUSSIAN fits to the distribution confirm the reproduction of the input values within 1σ . Note that only very few datapoints were available for the fits, because the distributions overwhelmingly converge into a single bin at ± 0.5 , hence the large errors on the fit parameters.

Bibliography

- [Afz19] F. N. Afzal, *Measurement of the beam and helicity asymmetries in the reactions $\gamma p \rightarrow p\pi^0$ and $\gamma p \rightarrow p\eta$* ,
PhD thesis: Rheinische Friedrich-Wilhelms-Universität Bonn, 2019,
URL: <https://hdl.handle.net/20.500.11811/8064>
(cit. on pp. 7, 9, 11, 12, 15, 17).
- [Leo94] W. R. Leo,
Techniques for Nuclear and Particle Physics Experiments, A How-to Approach, vol. 2,
Springer-Verlag Berlin Heidelberg GmbH, 1994 (cit. on pp. 8, 13, 14).
- [Hei54] W. Heitler, *The Quantum Theory of Radiation*, Oxford University Press, 1954
(cit. on p. 8).
- [Dem10] W. Demtröder, *Experimentalphysik 3, Atome, Moleküle, Festkörper*, vol. 4,
Springer-Verlag Berlin Heidelberg New York, 2010 (cit. on p. 8).
- [Nat+03] F. Natter, P. Grabmayr, T. Hehl, R. Owens and S. Wunderlich, *Monte Carlo simulation and analytical calculation of coherent bremsstrahlung and its polarisation*,
Nuclear Instruments and Methods in Physics Research Section B: Beam Interactions with Materials and Atoms **211** (2003) 465 (cit. on p. 9).
- [Els+09] D. Elsner et al., *Linearly polarised photon beams at ELSA and measurement of the beam asymmetry in π^0 photoproduction off the proton*,
The European Physical Journal A **39** (2009) 373,
URL: <https://doi.org/10.1140/2Fepja%2F12008-10708-1> (cit. on p. 9).
- [Kam10] S. Kammer, *Strahlpolarimetrie am CBELSA/TAPS Experiment*,
PhD thesis: Rheinische Friedrich-Wilhelms-Universität Bonn, 2010,
URL: <https://hdl.handle.net/20.500.11811/4539> (cit. on p. 9).
- [For10] K. Fornet-Ponse,
Die Photonenmarkierungsanlage für das Crystal-Barrel/TAPS-Experiment an ELSA,
PhD thesis: Rheinische Friedrich-Wilhelms-Universität Bonn, 2010,
URL: <https://hdl.handle.net/20.500.11811/4507> (cit. on p. 10).
- [Har08] J. Hartmann, *Zeitkalibrierung und Photonenflussbestimmung für das Crystal-Barrel-Experiment and ELSA*,
Diploma thesis: Rheinische Friedrich-Wilhelms-Universität Bonn, 2008
(cit. on pp. 10, 11, 13–15).
- [Wal] D. Walther, *Crystal Barrel, A 4π photon spectrometer*,
URL: <https://www.cb.uni-bonn.de> (visited on 27/09/2021) (cit. on pp. 10, 14).

Bibliography

- [Ham09] C. Hammann, *Aufbau eines Flüssigwasserstofftargets zur Durchführung von Kalibrationsmessungen am Crystal-Barrel Experiment an ELSA*, Diploma thesis: Rheinische Friedrich-Wilhelms-Universität Bonn, 2009 (cit. on pp. 10, 11).
- [Fös00] A. Fösel, *Entwicklung und Bau des Innendetektors für das Crystal Barrel Experiment an ELSA/Bonn*, PhD thesis: Friedrich-Alexander-Universität Erlangen-Nürnberg, 2000 (cit. on p. 11).
- [Suf+05] G. Suft et al., *A scintillating fibre detector for the Crystal Barrel experiment at ELSA*, Nucl. Instrum. Meth. A **538** (2005) 416 (cit. on p. 11).
- [PDG] PDG, *Atomic and Nuclear Properties*, URL: <https://pdg.lbl.gov/2022/AtomicNuclearProperties/index.html> (visited on 04/08/2022) (cit. on pp. 11, 13, 14).
- [Ake+92] E. Aker et al., *The Crystal Barrel spectrometer at LEAR*, Nucl. Instrum. Meth. A **321** (1992) 69 (cit. on pp. 12, 13).
- [Urb17] M. Urban, *Design eines neuen Lichtpulsersystems sowie Aufbau und Inbetriebnahme der neuen APD Auslese für das Crystal-Barrel-Kalorimeter*, PhD thesis: Rheinische Friedrich-Wilhelms-Universität Bonn, 2017 (cit. on pp. 12, 13).
- [Jun04] J. Junkersfeld, *Kalibration des Crystal-Barrel-ELSA Detektors mit Hilfe der Reaktion $\gamma p \rightarrow p\pi^0$* , Diploma thesis: Rheinische Friedrich-Wilhelms-Universität Bonn, 2004 (cit. on p. 13).
- [Bet30] H. Bethe, *Zur Theorie des Durchgangs schneller Korpuskularstrahlen durch Materie*, Annalen der Physik **397** (1930) 325, eprint: <https://onlinelibrary.wiley.com/doi/pdf/10.1002/andp.19303970303>, URL: <https://onlinelibrary.wiley.com/doi/abs/10.1002/andp.19303970303> (cit. on p. 13).
- [Hon14] C. Honisch, *Design, Aufbau und Test einer neuen Ausleseelektronik für das Crystal-Barrel-Kalorimeter*, PhD thesis: Rheinische Friedrich-Wilhelms-Universität Bonn, 2014 (cit. on p. 13).
- [Wen04] C. Wendel, *Entwicklung eines Szintillations-Detektors zur Identifikation geladener Teilchen im Crystal-Barrel Vorwärtsdetektor*, Diploma thesis: Rheinische Friedrich-Wilhelms-Universität Bonn, 2004 (cit. on p. 13).
- [Geh15] S. Gehring, *Test des Szintillationsdetektors zur Identifikation geladener Teilchen im Crystal-Barrel-Vorwärtsdetektor*, Bachelor thesis: Rheinische Friedrich-Wilhelms-Universität Bonn, 2015 (cit. on p. 13).
- [Gab+94] A. Gabler et al., *Response of TAPS to monochromatic photons with energies between 45 and 790 MeV*, Nuclear Instruments and Methods in Physics Research Section A: Accelerators, Spectrometers, Detectors and Associated Equipment **346** (1994) 168, ISSN: 0168-9002, URL: <https://www.sciencedirect.com/science/article/pii/0168900294907013> (cit. on pp. 13, 14).

-
- [Str96] H. Ströher, *Electromagnetic and Hadronic Probes of Nuclear Matter: Portrait of the European Photon Detector TAPS*, Nuclear Physics News **6** (1996) 7, eprint: <https://doi.org/10.1080/10506899609411060>, URL: <https://doi.org/10.1080/10506899609411060> (cit. on p. 13).
- [Nov91] R. Novotny, *The BaF/sub 2/ photon spectrometer TAPS*, IEEE Transactions on Nuclear Science **38** (1991) 379 (cit. on p. 13).
- [Kai07] D. Kaiser,
Aufbau und Test des Gas- Čerenkov-Detektors für den Crystal-Barrel-Aufbau an ELSA, Diploma thesis: Rheinische Friedrich-Wilhelms-Universität Bonn, 2007 (cit. on p. 14).
- [McG08] W. McGehee, *The Gamma Intensity Monitor of the Crystal-Barrel-Experiment*, Bachelor thesis: Massachusetts Institute of Technology, 2008 (cit. on p. 14).
- [Die08] J. Dielmann, *Entwicklung, Aufbau und Test eines Detektors zur Bestimmung des Photonenflusses an der Bonner Photonenmarkierungsanlage*, Diploma thesis: Rheinische Friedrich-Wilhelms-Universität Bonn, 2008 (cit. on p. 15).
- [Win06] A. Winnebeck, *Entwicklung und Implementierung eines universellen, FPGA basierten Triggermoduls für das Crystal-Barrel-Experiment and ELSA*, Diploma thesis: Rheinische Friedrich-Wilhelms-Universität Bonn, 2006 (cit. on p. 15).
- [Hof18] P. Hoffmeister,
Das Datenerfassungssystem für das Crystal-Barrel/TAPS-Exoeriment an ELSA, PhD thesis: Rheinische Friedrich-Wilhelms-Universität Bonn, 2018 (cit. on p. 15).
- [Fle01] H. Flemming, *Entwurf und Aufbau eines Zellularlogik-Triggers für das Crystal-Barrel-Experiment an der Elektronenbeschleunigeranlage ELSA*, PhD thesis: Rheinische Friedrich-Wilhelms-Universität Bonn, 2001 (cit. on p. 15).
- [Sch+] C. Schmidt et al., *Extended Pluggable Object-oriented Root Analysis*, URL: <https://explora.cb.uni-bonn.de> (visited on 10/08/2022) (cit. on p. 16).
- [BR97] R. Brun and F. Rademakers, *ROOT — An object oriented data analysis framework*, Nucl. Instrum. Meth. A **389** (1997) 81, ISSN: 0168-9002, URL: <https://www.sciencedirect.com/science/article/pii/S016890029700048X> (cit. on p. 16).
- [MU49] N. Metropolis and S. Ulam, *The Monte Carlo Method*, Journal of the American Statistical Association **44** (1949) 335, PMID: 18139350, eprint: <https://www.tandfonline.com/doi/pdf/10.1080/01621459.1949.10483310>, URL: <https://www.tandfonline.com/doi/abs/10.1080/01621459.1949.10483310> (cit. on p. 16).
- [Bru+87] R. Brun, F. Bruyant, M. Maire, A. C. McPherson and P. Zanarini, *GEANT3*, (1987) (cit. on p. 16).
- [Kal11] F. Kalischewski, *Development of a new simulation for the CBELSA/TAPS experiment using Virtual Monte Carlo*, Diploma thesis: Rheinische Friedrich-Wilhelms-Universität Bonn, 2011 (cit. on p. 16).

Bibliography

- [AKN+] A. Anisovich, E. Klempt, V. Nikonov et al., *Bonn-Gatchina Partial Wave Analysis*, URL: <https://pwa.hiskp.uni-bonn.de/> (visited on 10/08/2022) (cit. on p. 16).
- [Ani+12] A. V. Anisovich et al.,
Properties of baryon resonances from a multichannel partial wave analysis,
The European Physical Journal A **48** (2012),
URL: <https://doi.org/10.1140%2Fepja%2F12012-12015-8> (cit. on p. 16).
- [Mah22] P. Mahlberg, *Thesis in Preparation*,
Rheinische Friedrich-Wilhelms-Universität Bonn, 2022 (cit. on p. 16).
- [Sta22] Stan development team, *Stan Modeling Language Users Guide and Reference Manual*, vol. 2.29, 2022, URL: <https://mc-stan.org> (cit. on p. 17).
- [RP22] G. van Rossum and the Python development team,
The Python Language Reference, Release 3.10.5, 2022,
URL: <https://docs.python.org/3.10/reference/index.html> (cit. on p. 17).
- [McK10] W. McKinney, “Data Structures for Statistical Computing in Python”,
Proceedings of the 9th Python in Science Conference,
ed. by S. van der Walt and J. Millman, 2010 56 (cit. on p. 17).

List of Figures

1.1	Running coupling of QCD. The colored data points represent different methods to obtain a value for α_s . For more details it may be referred to [pdg].	2
1.2	Calculated nucleon (isospin $I = 1/2$) resonances compared to measurements. Left in each column are the calculations [bonnmodel], the middle shows the measurements and PDG rating [pdg]	3
1.3	FEYNMAN diagram for the s-channel photoproduction of pseudoscalar mesons, adapted from [Afz19]	4
2.1	Overview of the experimental hall of the CBELSA/TAPS experiment. The electron beam from ELSA enters at the top right. M. GRÜNER in [Afz19]	7
2.2	Illustration of the bremsstrahlung process: An electron e^- is deflected in the COLOUMB field of a nucleus in the radiator material. A photon γ is emitted and so the momentum q is transferred.	8
2.3	Left: Incoherent (green) and crystal (blue) bremsstrahlung intensities as a function of the photon energy. Right: The enhancement spectrum is given as the ratio of crystal to incoherent intensity spectrum. The dashed line at the bottom shows the calculated polarization degree. Both spectra are generated using ANB calculations. Taken from [Afz19].	9
2.4	The goniometer holds several radiators that can be inserted onto the beam axis (b). Also available is a MØLLER radiator [Wal].	10
2.5	Top-down view of the tagging system consisting of dipole magnet (red) and scintillating bars and fibers [For10]. Electrons are deflected by the magnet after the bremsstrahlung process.	10
2.6	Schematic overview of the liquid hydrogen target. Two tubes connected to a heat exchanger and the Kapton cell allow filling it with liquid hydrogen. M. GRÜNER in [Afz19].	11
2.7	The inner detector with three layers of scintillating fibers. The inner two layers are tilted with respect to the outer layer. D. WALTHER in [Afz19].	12
2.8	Crystal barrel calorimeter and forward detector are built such that they enclose the target and the inner detector. The forward detector consists of the first three rings (green base) of crystals which are additionally covered by plastic scintillators for charged particle identification. The definition of polar angle θ and azimuthal angle ϕ in the LAB system are indicated as well.D. WALTHER in [Urb17]	12
2.9	The MiniTAPS detector is made up of 216 BaF ₂ crystals (grey). In front of each crystal, plastic scintillators are mounted for charged particle information. Taken from [Wal].	14

2.10	The two detectors FluMo and GIM are used to monitor the photon flux at different reaction rates. D. WALTHER in [Afz19].	15
3.1	Distribution of event classes in $\eta' \rightarrow \gamma\gamma$ production	21
3.2	Time information of all final state particles and the beam photon for 3PED η' production	22
3.3	Reaction time t_r for 3PED and 2.5PED η' production. The yellow region indicate the sidebands while the purple colored interval is the selected prompt peak.	23
3.4	Coplanarity of the $p\eta'$ final state with all other cuts applied for the energy bin $1500 \text{ MeV} \leq E_\gamma < 1600 \text{ MeV}$. The vertical dashed lines show the cut ranges obtained from a gaussian fit to the data (open circles). The solid black histograms represent fitted MC data of $\eta' \rightarrow \gamma\gamma$	27
3.5	Polar angle difference of the $p\eta'$ final state with all other cuts applied for the energy bin $1500 \text{ MeV} \leq E_\gamma < 1600 \text{ MeV}$. The vertical dashed lines show the cut ranges obtained from a gaussian fit to the data (open circles). The solid black histograms represent fitted MC data of $\eta' \rightarrow \gamma\gamma$	28
3.6	Missing mass of the $p\eta'$ final state with all other cuts applied for the energy bin $1500 \text{ MeV} \leq E_\gamma < 1600 \text{ MeV}$. The vertical dashed lines show the cut ranges obtained from a fit to data (open circles) employing a NOVOSIBIRSK function. The solid colored histograms represent fitted MC data from relevant photoproduction reactions: in black η' , in green π^0 , in red η , in blue ω , in yellow $2\pi^0$, magenta $\pi^0\eta$. The turquoise histogram is the sum of all MC histograms.	29
3.7	Invariant mass of the $p\eta'$ final state with all other cuts applied for all energy and angular bins. The open circles represent the measured data, the solid colored histograms fitted MC data from relevant photoproduction reactions: in black η' , in green π^0 , in red η , in blue ω , in yellow $2\pi^0$ and in magenta $\pi^0\eta$. The turquoise histogram is the sum of all MC histograms.	30
3.8	Invariant mass of the $p\eta'$ final state with all other cuts applied for the energy bin $1500 \text{ MeV} \leq E_\gamma < 1600 \text{ MeV}$. The vertical dashed lines show the cut ranges obtained from a gaussian fit to the η' MC data (solid black histogram). The open circles represent the measured data, the solid colored histograms fitted MC data from relevant photoproduction reactions: in black η' , in green π^0 , in red η , in blue ω , in yellow $2\pi^0$ and in magenta $\pi^0\eta$. The turquoise histogram is the sum of all MC histograms.	30
3.9	Acceptance for the reaction $\gamma p \rightarrow p\eta'$ after all cuts that have been discussed so far for 2.5PED and 3PED events	31
3.10	Fraction of background events in the analyzed beam energy and angular bins.	32
3.11	Acceptance for possible background contributions	33
3.12	Generated energies of γ_3 and γ_4 in $2\pi^0$ and $\pi^0\eta$ photoproduction MC data. The threshold of 20 MeV is marked by a vertical red line. E_{γ_4} is shown on the top, E_{γ_3} is shown on the bottom of each figure.	35
3.13	E_γ^{gen} vs. E_γ^{rec} of γ_1 and γ_2 for $2\pi^0$ (top) and $\pi^0\eta$ (bottom) production. The slope $E_\gamma^{\text{gen}} = E_\gamma^{\text{rec}}$ is marked by a solid line.	37
3.14	Polar angle difference $\Delta\theta$ between γ_2 and γ_3 of the $\pi^0\eta$ final state.	38
3.15	Illustration of the misidentification process during reconstruction. Enumeration of photons is now arbitrary.	38

3.16	Generated CMS angle $\cos \theta_{\text{gen.}}$ vs. reconstructed CMS angle $\cos \theta_{\text{rec.}}$ for both background reactions. The slope $\cos \theta_{\text{gen.}} = \cos \theta_{\text{rec.}}$ is indicated by the solid line.	39
3.17	Detector hits of the recoil proton, as obtained from MC data for the production of η' , $2\pi^0$ and $\pi^0\eta$. CB: Crystal Barrel, FW: forward dector, MT: MiniTAPS	41
3.18	Difference in measured and calculated beam energy. Data points are shown as open circles, MC data as solid histograms: in black η' , in green π^0 , in red η , in blue ω , in yellow $2\pi^0$ and in magenta $\pi^0\eta$. The turquoise histogram is the sum of all MC histograms.	42
3.19	Invariant mass spectrum passing different stages in the event selection process. In the end clear peaks for all possibly produced mesons are visible. The vertical lines indicate the mean cut ranges over all energy and angle bins.	43
3.20	Invariant mass spectrum passing different stages in the event selection process. In the end clear peaks for all possibly produced mesons are visible. Taken from [Afz19].	44
4.1	Left: Definition of angles α, ϕ, φ . Right: Photon momentum \vec{k} and polarization $\vec{\epsilon}$ define the beam polarization plane while the reaction plane is defined by the recoil proton p and produced meson M	37
4.2	Posterior predictive checks $p(A_{\text{rep}} A)$ from a BAYESIAN fit to the event yield asymmetries for six toy Monte Carlo bins are shown as distributions. The data points in the upper plot are the asymmetry $A(\phi)$, which was additionally fitted using a χ^2 fit (solid line). The goodness of fit is shown using p -values, which give the fraction $T(A_{\text{rep}} > A)$ of replicated samples greater than the original measured value, with propagated statistical error bars on the bottom of each plot. The expected mean value of $T(A_{\text{rep}} > A) = 0.5$ is indicated by the dashed line.	46
4.3	p values of all toy Monte Carlo bins. They are centered around their mean at 0.5, which is indicated by the dashed line, and show no bias towards higher or lower values, thus confirming an adequate fit.	47
4.4	Left: Combined posterior distributions of all 10000 fits normalized by their respective standard deviation. Right: Unaltered combined posterior distributions of all 10000 fits. A GAUSSIAN fit was performed to determine mean μ and standard deviation σ of the distributions with results given on top.	47
4.5	Left: relative error $\frac{\sigma_{\text{MCSE}}}{\text{median}[p(\Sigma y)]}$ Right: \widehat{R} associated with the fit parameter Σ . Both are shown for all 10000 fits. The critical values that should not be exceeded are marked by dashed lines.	48
4.6	Combined posteriors for the beam asymmetries Σ and Σ^{bkg} from all 1000 event based fits. Left: Residuals Ξ Right: Unnormalized posterior distributions. A GAUSSIAN fit is performed on the distributions with results for mean μ and standard deviation σ on top.	50
4.7	Combined posterior probabilities using the <i>pooled likelihood</i> approach. Left: Signal beam asymmetry, Right: background beam asymmetry. Mean and standard deviation as obtained from a Gaussian fit are shown on top	51
4.8	Left: relative error $\frac{\sigma_{\text{MCSE}}}{\text{median}[p(\Sigma y)]}$ Right: \widehat{R} associated with the fit parameter Σ . Both are shown for all 1000 fits. The critical values that should not be exceeded are marked by dashed lines.	51

4.9	Posterior predictive check using the draws of the detector coefficients a and b . Points with error bars are the polarization weighted sum of event yields. The dashed line is the mean of the predictive values while the solid opaque lines are representative of one simulation draw $a^{(s)}, b^{(s)}$	52
4.10	Posterior predictive checks $p(A_{\text{rep}} A)$ from a BAYESIAN fit to the event yield asymmetries for all angular bins of the energy bin $1250 \text{ MeV} \leq E_\gamma < 1310 \text{ MeV}$. The data points in the upper plot are the asymmetry $A(\phi)$, which was additionally fitted using a χ^2 fit (solid line). The goodness of fit is shown using p -values, which give the fraction $T(A_{\text{rep}} > A)$ of replicated samples greater than the original measured value, with propagated statistical error bars on the bottom of each plot. The expected mean value of $T(A_{\text{rep}} > A) = 0.5$ is indicated by the dashed line.	54
4.11	p values generated using all fits. They are centered around their mean at 0.5, which is indicated by the dashed line, and show no bias towards higher or lower values, thus confirming an adequate fit.	55
4.12	Left: relative error $\frac{\sigma_{\text{MCSE}}}{\text{median}[p(\Sigma y)]}$ Right: \widehat{R} associated with the fit parameter Σ . Both are shown for all $11 \cdot 12$ binned fits to the asymmetry $A(\phi)$. The critical values that should not be exceeded are marked by dashed lines.	55
4.13	Left: relative error $\frac{\sigma_{\text{MCSE}}}{\text{median}[p(\Sigma y)]}$ Right: \widehat{R} associated with the fit parameter Σ . Both are shown for all $11 \cdot 12$ unbinned fits. The critical values that should not be exceeded are marked by dashed lines.	56
4.14	Posterior predictive check using the draws of the detector coefficients a and b for the kinematic bin $1250 \text{ MeV} \leq E_\gamma < 1310 \text{ MeV}, 0 \leq \cos \theta < 0.17$. Points with error bars are the polarization weighted sum of event yields. The dashed line is the mean of the predictive values while the solid opaque lines are representative of one simulation draw $a^{(s)}, b^{(s)}$	57
4.15	Final results for the beam asymmetry Σ in η photoproduction off the proton for all kinematic bins obtained with BAYESIAN methods. They are compared with the results of a least squares fit and an unbinned fit as given in reference [Afz19]. All results agree within statistical error bars or within the widths of marginal posterior distributions.	59
4.16	Normalized residuals (left) and unaltered distribution (right) of all 10000 fits for the beam asymmetry $\Sigma = (1 - \delta) \cdot \Sigma_1 + \delta \cdot \Sigma_2$. GAUSSIAN fits are performed with results given on top of each plot.	61
4.17	Normalized residuals (left) and unaltered distribution (right) of all 10000 fits for the background beam asymmetry Σ_t^{bkg} . GAUSSIAN fits are performed with results given on top of each plot.	62
4.18	Fitted efficiency function (red line) applied to the polarization weighted sum of event yields (data points) for one toy Monte Carlo bin. 12 bins in ϕ are built for demonstration.	62
4.19	Combined (added) posteriors of all 1000 fits. Left: Signal beam asymmetry Σ_1 Right: Background beam asymmetry Σ_t^{bkg} . A GAUSSIAN fit is performed with results given on top.	63
4.20	Combined (added) posteriors of all fits for the fit parameter Σ_2^{true} . A GAUSSIAN fit is performed which reproduces exactly the values that were used for the simulations.	64

4.21	MCMC diagnostics for the event based BAYESIAN fit. Left: MCSE, Right: \widehat{R} -value. The critical values not to be exceeded are marked by the dashed lines.	65
4.22	Posterior predictive checks of one toy Monte Carlo bin using the draws from the marginal posteriors of the detector coefficients a, b (opaque blue lines). The mean values are marked by the dashed line and follow the distribution of the data points which are the polarization weighted sum of event yields, using 12 ϕ bins.	65
4.23	Final results for the beam asymmetry Σ in η' photoproduction. Two sets of results are shown: The dark blue distributions and orange data points with errorbars are obtained with an unbinned fit that does not consider any background contributions. The light blue distributions and data points are obtained with the modified BAYESIAN fit and by correcting the point estimates according to Equation (4.42), respectively. All errors are statistical errors only.	67
4.24	Results for the additionally fitted Σ_2^{true} (distributions) compared with the underlying data points [Mah22] with statistical errors. The error bars on average cover 1σ of the distributions, indicating a successful fit. All errors are statistical errors only.	68
4.25	MCMC diagnostics for the event based BAYESIAN fit. Left: MCSE, Right: \widehat{R} -value. The critical values not to be exceeded are marked by the dashed lines.	69
4.26	Posterior predictive checks of the kinematic bin $1700 \text{ MeV} \leq E_\gamma < 1800 \text{ MeV}, 0.67 \leq \cos \theta < 1$ using the draws from the marginal posteriors of the detector coefficients a, b (opaque blue lines). The mean values are marked by the dashed line and follow the distribution of the data points which are the polarization weighted sum of event yields, using 12 ϕ bins.	69
4.27	Final results for the beam asymmetry $\Sigma_{\eta'}$ for all energy and angular bins. Only the corrected results from the unbinned maximum likelihood fit and distributions from the modified BAYESIAN fit are shown. The bottom of each plot indicates the systematic error as gray bars. It was determined as previously discussed.	71
5.1	Results for the beam asymmetry $\Sigma_{\eta'}$ (orange errorbars and distributions) compared with the results for the energy bins $E_\gamma = 1569 \text{ MeV}, E_\gamma = 1676 \text{ MeV}, E_\gamma = 1729 \text{ MeV}$ reported in reference [collins] (black errorbars). Systematical errors are shown as grey bars.	74
5.2	Results for the beam asymmetry $\Sigma_{\eta'}$ (orange errorbars and distributions) compared with PWA solutions: etaMAID [etaMAID](dashed black line), . . . The errorbars only depict statistical error, the systematic error is shown as grey bars.	76
A.1	Example .xml file that was used to call the plugin CBTetaprimeanalysis.cpp (line 20) with several self defined options.	75
A.2	Example .stan file that can be used to perform a simple linear fit.	76
B.1	Coplanarity $\Delta\phi$ for all energy and angular bins. Data points are displayed as open circles, scaled Monte Carlo data belonging to η' photoproduction is displayed as solid histogram. The determined cut ranges are indicated by the dashed red lines.	79
B.1	Coplanarity $\Delta\phi$ for all energy and angular bins. Data points are displayed as open circles, scaled Monte Carlo data belonging to η' photoproduction is displayed as solid histogram. The determined cut ranges are indicated by the dashed red lines.	80

B.2	Polar angle difference $\Delta\theta$ for all energy and angular bins. Data points are displayed as open circles, scaled Monte Carlo data belonging to η' photoproduction is displayed as solid histogram. The determined cut ranges are indicated by the dashed red lines.	81
B.2	Polar angle difference $\Delta\theta$ for all energy and angular bins. Data points are displayed as open circles, scaled Monte Carlo data belonging to η' photoproduction is displayed as solid histogram. The determined cut ranges are indicated by the dashed red lines.	82
B.3	Missing mass m_x for all energy and angular bins. Data points are displayed as open circles, scaled Monte Carlo data belonging to η' (black), $2\pi^0$ (yellow) and $\pi^0\eta$ (magenta) photoproduction is displayed as solid histogram while their sum is displayed as turquoise histogram. The determined cut ranges are indicated by the dashed red lines.	83
B.3	Missing mass m_X for all energy and angular bins. Data points are displayed as open circles, scaled Monte Carlo data belonging to η' (black), $2\pi^0$ (yellow) and $\pi^0\eta$ (magenta) photoproduction is displayed as solid histogram while their sum is displayed as turquoise histogram. The determined cut ranges are indicated by the dashed red lines.	84
B.4	Invariant mass m_{meson} for all energy and angular bins. Data points are displayed as open circles, scaled Monte Carlo data belonging to η' (black), $2\pi^0$ (yellow), $\pi^0\eta$ (magenta), π^0 (green) and ω (blue) photoproduction is displayed as solid histogram while their sum is displayed as turquoise histogram. The determined cut ranges are indicated by the dashed red lines.	85
B.4	Invariant mass m_{meson} for all energy and angular bins. Data points are displayed as open circles, scaled Monte Carlo data belonging to η' (black), $2\pi^0$ (yellow), $\pi^0\eta$ (magenta), π^0 (green) and ω (blue) photoproduction is displayed as solid histogram while their sum is displayed as turquoise histogram. The determined cut ranges are indicated by the dashed red lines.	86
C.1	Fit performance in dependence of the number of bins. Left axis shows the mean μ of the distribution of the normalized residuals ξ , right axis shows the mean χ^2 of all fits. Squares simulate fits with statistics similar to the $\gamma p \rightarrow p\eta' \rightarrow p\gamma\gamma$ final state, triangles statistics similar to the $\gamma p \rightarrow p\eta \rightarrow p\gamma\gamma$ and final state, pentagons statistics similar to the $\gamma p \rightarrow p\pi^0 \rightarrow p\gamma\gamma$. Dotted red line indicates the ideal value of $\chi^2 = 1$, while the dashed blue line indicates the ideal mean of the normalized residuals at $\mu = 0$	88
D.1	Combined posteriors of all 1000 fits without truncation for the signal beam asymmetry Σ_1 and the background beam asymmetry Σ_t . Left: normalized residuals Ξ , Right: unaltered added posterior distributions. GAUSSIAN fits have been performed with results given on top of each plot.	90
D.2	Posterior distributions of Σ_1 (left) and Σ_t (right) combined in an independent likelihood pool. GAUSSIAN fits to the distribution confirm the reproduction of the input values within 1σ . Note that only very few datapoints were available for the fits, because the distributions overwhelmingly converge into a single bin at ± 0.5 , hence the large errors on the fit parameters.	91

List of Tables

1.1	Summary of the particles of the SM	1
1.2	Allowed quantum numbers for the intermediate resonance state N^*/Δ^*	4
2.1	Summary of the key parameters of the 2013 beam time at CBELSA/TAPS taken for the measurement of the beam asymmetry Σ . Taken from [Afz19].	17
3.1	The five most probable decay modes of the η and η' meson. The most probable further decay with according branching ratio is shown in brackets.[pdg]	19
3.2	Examined MC reactions that were used in sum for the fit	25
3.3	Fit functions and cut ranges for each kinematic variable	26
3.4	Total cross sections σ in the energy range 1500 to 1800 MeV, branching ratios (BR) to $n\gamma$ final states, maximum acceptance \tilde{A} for signal and possible background contributions as well as the expected signal to background ratio R . References [2pi0_cs] and [pi0eta_cs] give the cross sections only up to roughly 1500 MeV, the given values are thus upper bounds. For the same reason, from reference [3pi0cs] only a lower bound can be estimated. For all other reactions a rough mean over the energy bins of interest is built. If the references provide only differential cross sections a crude integration in each angular bin is performed. In case only very few ($O(10^1)$) decays pass event selection, the acceptance is built in one global bin only for the respective reactions. This is indicated by the horizontal line.	34
3.5	Relative loss in signal and background events if a cut on ΔE is applied.	40
4.1	Summary of the complete setting of all toy Monte Carlo experiments for the event based fit. Values and table layout adapted from [Afz19].	49
4.2	Summary of the complete setting of all toy Monte Carlo experiments for the event based fit. Table layout adapted from [Afz19].	60